SAO-AXAF-DR-94-088
Data Type: 3
Rev "A"
June 1994

Advanced X-Ray Astrophysics Facility (AXAF)

Mission Support

NAS8-36123

INTERIM
IN-89-CR

Performance Report:

HRMA Calibration Handbook:

EKC Gravity Compensated XRCF Models

Prepared in accordance with DRD# 784MA-002

Principal Investigator

Dr. H. D. Tananbaum

Prepared for:
George C. Marshall Space Flight Center
National Aeronautics and Space Administration
Marshall Space Flight Center, AL 35812

Smithsonian Astrophysical Observatory
60 Garden Street
Cambridge, MA 02138

The Smithsonian Astrophysical Observatory
is a member of the
Harvard-Smithsonian Center for Astrophysics

SAO-AXAF-DR-94-088
Data Type: 3
Rev "A"
June 1994

Advanced X-Ray Astrophysics Facility (AXAF)

Mission Support

NAS8-36123

Performance Report:

HRMA Calibration Handbook:

EKC Gravity Compensated XRCF Models

Prepared in accordance with DRD# 784MA-002

Principal Investigator

Dr. H. D. Tananbaum

Prepared for:
George C. Marshall Space Flight Center
National Aeronautics and Space Administration
Marshall Space Flight Center, AL 35812

Smithsonian Astrophysical Observatory
60 Garden Street
Cambridge, MA 02138

Smithsonian Institution
Astrophysical Observatory

Title: Performance Report:
HRMA Calibration Handbook
EKC Gravity Compensated
XRCF Models

Date: 6 Jun 1994

Document No.: SAO-AXAF-DR-94-088

DRD No.: 784MA-002

Prepared by: D.Jerius
J.Hughes

Data Type: 3

Filename: (c:784ma002.088)

Revision: "A"

APPROVAL SIGNATURES

F. Cocuzzo
Program Manager

6/6/94
Date

Smithsonian Institution
Astrophysical Observatory

REVISION HISTORY

Title: Performance Report:
HRMA Calibration Handbook:
EKC Gravity Compensated
XRCF Models

Date: 6 Jun 1994

Document No.: SAO-AXAF-DR-94-088

DR No.: 784MA-002

Prepared by: D.Jerius
J.Hughes

Data Type: 3

Filename: (c:784ma002.088)

Revision: "A"

Revision Record

Revision	Date	DCO No.	Affected Pages
"A"	6 June 94	-------	Initial Release

Contents

Appendices:

Tables

Figures

1. Introduction and Motivation

Many organizations are contributing to the AXAF calibration effort and, in the course of their work, often require data on the expected performance of the AXAF high resolution mirror assembly (HRMA) to properly plan or assess calibration activities. In an effort to provide such information to the AXAF project, the SAO Mission Support Team (MST) has decided to prepare the HRMA Calibration Handbook. This document, consisting of hardcopy printout of explanatory text, figures, and tables, represents one incarnation of the HRMA Calibration Handbook. However, as we have envisioned it, the Handbook also consists of electronic versions of this hardcopy printout (in the form of postscript files), the individual scripts which produced the various figures and the associated input data, the model raytrace files, and all scripts, parameter files, and input data necessary to generate the raytraces. These data are all available electronically as either ASCII or FITS files. The Handbook is intended to be a living document and will be updated as new information and/or fabrication data on the HRMA are obtained, or when the need for additional results are indicated. We also intend that the Handbook should document the status of our HRMA model in order to facilitate comparison with future versions of both our model and raytrace models being developed by other organizations on the AXAF Team. Finally we note that SAO provided a similar document before the VETA-I test (Hughes and Podgorski 1990) which proved to be quite valuable to the planning and execution of that test.

The SAO MST is developing a high fidelity HRMA model, consisting of analytical and numerical calculations, computer software, and databases of fundamental physical constants, laboratory measurements, configuration data, finite element models, AXAF assembly data, and so on. This model serves as the basis for the simulations presented in the Handbook. The "core" of the model is the raytrace package OSAC (Glenn & Noll 1982, version 5.0), which we have substantially modified and now refer to as SAOsac.

One major structural modification to the software has been to utilize the UNIX binary pipe data transport mechanism for passing rays between program modules. This change has made it possible to simulate rays which are distributed randomly over the entrance aperture of the telescope. It has also resulted in a highly efficient system for tracing large numbers of rays. In one application to date (the analysis of VETA-I ring focus data) we have employed

2×10^7 rays (Zhao *et al.* 1994), a substantial improvement over the limit of 1×10^4 rays in the original OSAC module.

A second major modification is the manner in which SAOsac incorporates low spatial frequency surface errors into the geometric raytrace. The original OSAC included the ability to use Legendre-Fourier polynomials to describe deviations from the basic optical prescription. To this we have added bicubic splines to address a deficiency in the handling of the sharper deformations in the areas of mirror support pads. SAO has developed software (TRANSFIT) to translate the most common Finite Element Analysis models into these forms for incorporation into the raytrace program.

2. Description of Model

A complete HRMA model consists of several components:

- a finite element model (FEM) of the mirror support structure and an analysis of the deformations induced in the mirrors by it
- mechanical models of the thermal pre- and post- collimators
- mechanical models of the ghost ray baffles
- mechanical models of the Central Aperture Plate (CAP)
- a prescription for the gross mirror geometry
- a model of the mirror surface imperfections (e.g., surface micro-roughness) and alignment errors (e.g., relative tilts between parabola-hyperbola mirror pairs)
- models of surface contamination (e.g., dust)

Our intention for this first release of the HRMA Calibration Handbook is to focus on the deformations induced in the HRMA by the 1-g off-loaded mount at the XRCF as calculated by EKC. Thus the present model includes only the FEM and the gross mirror geometries. It includes neither obstructions nor vignetting by the support structures, the thermal collimators or other baffles. We have included no intrinsic HRMA surface error terms, either high frequency (such as surface micro-roughness) or low frequency (such as sag or mirror alignment errors). This omission allows us to highlight the structure in the images due to

the FEM, which, in fact, is a major contributor to the size and shape of the image core. Furthermore it facilitates direct and detailed comparison with the results of FEMs calculated by other groups. SAO, in particular, is currently preparing a FEM model of the off-loaded HRMA at the XRCF and when it becomes available, we will reproduce the results given here with it. A comparison of the results from the EKC and SAO FEMs will provide an estimate of the range of X-ray performance expected based on (some measure of) the uncertainty in our ability to predict the induced gravitational deformations. However, the reader should keep in mind that the images we present here appear considerably sharper than will be the case during the actual calibration test and that care should be taken in further interpreting these results out of the context for which they are intended. We plan to include intrinsic HRMA surface error terms in one of the next releases of this document.

The FEM is derived from the EKC model current as of 23 September 1993. It incorporates gravity compensation with off-loading via the GSE off-loading system (off-loading at the CAP). The EKC NASTRAN (FEM) spans 180° (a semi-circle with the diameter vertical) and was reflected across the vertical axis to create a full 360° structure. This was fit by B-splines using TRANSFIT by M. Freeman (SAO). Because the FEM is symmetric, special care was taken to ensure that the TRANSFIT spline fit retained this symmetry. This HRMA model does not include contributions by the fore and aft structures. Future versions will include these, as well as alignment errors, assembly strain, thermal distortions, epoxy shrinkage, and material variations. Appendix D lists the locations of the particular files used in this analysis.

The nominal mirror geometry is that denoted by "EK05lvs" (Van Speybroeck 1989). The mirrors are assumed to be coated with Ir, with reflectivities given by Henke (1993). An index of the models is presented in Table 2.1.

Table 2.1: Model descriptions

Model	Description
xrcf	EKC 1G, off-load compensated mechanical model, mirror prescription EK05lvs

The X-ray source at the XRCF is modeled as a monochromatic point source at a distance of 528.74 meters from the HRMA's entrance aperture. The source provides uniform coverage

of an annular entrance aperture at the front of the HRMA. Future models will provide a more realistic polychromatic, spatially resolved, and non-uniformly filling source.

The photons are accumulated at the focal plane by both a "perfect" detector and a detector similar to the high speed imager (HSI) being developed by SAO for the HXDS. The HSI is modeled as having a Gaussian spatial resolution with a 18 μ FWHM, sampled with 6.45 μ square pixels. It is assumed that the collecting area of the HSI is equal to its spatial extent (i.e., there are no gaps between the pores), and that it has a perfect quantum efficiency. Future models will include the "dead" gaps between pores, as well as their tilt and hexagonal spatial distribution.

The location of the focal plane is that denoted as the *global optimal focus* position as determined by the SAOsac focus module. This focal position tracks the three dimensional minimum RMS blur circle of the ray bundle. The detector's imaging surface is assumed to be perpendicular to the HRMA optical axis. Future editions will explore alternate, more experimentally relevant descriptions of the focal plane.

Due to the finite distance of the XRCF X-ray source from the HRMA, the minimal annular entrance apertures required for complete illumination of the paraboloids are somewhat larger than for an on-axis source at infinity. Off-axis sources enlarge these annuli dramatically. In a faithful model of the HRMA the entrance apertures would be defined by the thermal pre-collimator, the forward edges of the mirrors, the finite distance to the source, and the source's angular extent. In the present study we have simplified this a great deal, and, to ensure complete illumination, have chosen apertures which are substantially larger than the actual entrance apertures. Increased sophistication in future models of the HRMA and XRCF systems will allow us to use more realistic apertures and (as a pleasant side effect) increase the throughput of our system. Note that the choice of an entrance aperture does not invalidate any effective area measurements. Table 2.2 compares nominal apertures (i.e. for an on-axis source at infinity) with those used in these simulations. The contribution of each shell to the geometrical effective area of the HRMA for an on-axis source at the XRCF is described in Table 2.3.

Simulated rays were distributed uniformly and randomly over an entrance aperture with a density of 20 photons/mm^2. This translates into roughly 2×10^6 rays at the focal plane for the on-axis case.

Table 2.2: HRMA Entrance Apertures

MP	R_i (mm) *nominal*	R_o (mm) *nominal*	Area (cm^2) *nominal*	R_i (mm) *used*	R_o (mm) *used*	Area (cm^2) *used*	Area Ratio *used / nominal*
1	600.35	612.69	470.479	552.47	612.69	2204.38	4.69
3	483.47	493.41	305.143	435.63	493.41	1686.38	5.53
4	426.85	435.63	237.869	379.11	435.63	1446.74	6.08
6	317.29	323.82	131.438	300.00	323.82	466.74	3.55

Table 2.3: Contributions to Geometrical Area for on-axis sources

MP	% Area
1	40.3
3	26.8
4	21.1
6	11.8

In order to minimize the computational burden of these calculations, we model the probabilistic reflection of photons from the mirrors by assigning each photon a unit weight at the entrance aperture and multiplying it by the photon's reflection probability at each surface. Only the weights are used in the analysis of the simulations. Note that we treat Poisson errors in the standard manner (as the square root of the weights) even though we utilize non-integral photons.

Table 2.4 indicates the combinations of model and source parameters simulated.

Table 2.4: Simulation parameters

HRMA model	Energy KeV	Azimuth ′	Elevation ′
xrcf	0.277	0.0	0.0
xrcf	0.277	0.0	15.0

3. Data Products

This handbook presents summaries of the data derived from simulations of the HRMA and HXDS. The data products are presented in Appendix A. A brief analysis of some of the data is presented in Appendix B. We present results for the performance of individual shells as well as for the full HRMA.

3.1. General characteristics

3.1.1. Coordinate System

The coordinate system used in this document is that used at the XRCF. We have chosen the origin of the system such that the x axis is the optical axis of a perfect, distortion free HRMA. The image of an on-axis object at infinity would thus lie at $z = 0$, $y = 0$. $x = 0$ is at the front edge of the paraboloids, and increases towards the focal plane. z and y complete a right-handed coordinate system, with z chosen by convention to be perpendicular to the local horizon, increasing towards the zenith. Future work will be based upon a coordinate system based upon fiducial marks machined into the CAP. It is uncertain at press time what the relationship between that system and the one used here will be.

3.1.2. Focal Plane positions

The optimal focus position is determined independently for each of the shells and the full HRMA. The axial positions differ for each of these cases, being relatively similar for on-axis sources, but varying dramatically off-axis. The global optimal focus for the HRMA in the off-axis case is essentially a weighted average of all four shells, and thus the image is less well focussed than are those of the individual shells. As the shells' effective areas vary with the incident photons' energies, the focal position for the HRMA also changes with energy.

3.1.3. Image Centers

Several of the data products are radially averaged quantities and are thus sensitive to the determination of the center of the focal plane ray distribution. As with any asymmetric distribution, the definition of its center may be ambiguous. Here we distinguish between the operational definition of a center and its desired properties. For example, one can define the algorithm for determining the center in one of the following manners:

- the *centroid*

$$y_c = \frac{\sum_i y_i w_i}{\sum_i w_i} \tag{3.1a}$$

$$z_c = \frac{\sum_i z_i w_i}{\sum_i w_i} \tag{3.1b}$$

- the *iteratively clipped* center. This is determined by calculating the centroid of a sample of the rays whose distance from an initial center is less than a given multiple of the standard deviation of the distance for the entire set of rays. This process is repeated, using the newly determined center as the basis for the next iteration, until the change in the center is less than some tolerance.
- an *experimental* center, which can be determined experimentally (using pin-holes, for instance) at the XRCF.

The resultant center may not correspond to what is probably the *desired* center, the *peak* or "modal location" of the distribution, for a number of reasons.

In the case of an on-axis source, the resultant focal plane distribution is quite peaked, but asymmetries due to gravity (even after compensation) and dust or high frequency mirror errors may produce substantial tails in the distribution which result in large lever arms in Eq. (3.1), shifting the centroid. Off-axis sources are (by definition, but also practically) not in focus; the central peak is muted and may indeed be non-existent, given a large enough off-axis deviation.

Our initial attempt at determining the center uses the clipped centering algorithm. Our current implementation has not shown itself to be more capable at locating the peak than the centroid. (See Table A.1 for a quantitative comparison.) Not much effort has so far been lavished upon this, as the analyses we present here are not critically dependent upon the center. Future efforts will concentrate upon determining the limitations of this method, as

well as defining algorithms which fall in the last of the above categories, namely those which are readily determined experimentally at the XRCF.

3.2. Specific Products

3.2.1. Grayscale Images

We present two sets of grayscale images. One shows the photon weight distribution binned in relatively small bins (1μ for on-axis images, 10μ for off-axis images), the other that imaged by our model HSI. In both cases the logarithm of the summed photon weights is shown.

3.2.2. Fractional Encircled Energy

The fraction of the total energy within a circular region is determined by binning the photons in annuli with widths of 0.1 μ. Image centers are determined using the clipped center algorithm of §3.1.3. The plots indicate results based upon these centers as well as centers offset by 1 μ in the cardinal directions. We have tabulated values of the encircled energy at radii of interest to the HXDS science staff.

3.2.3. HSI photon sampling

The relative distribution of photon weights per pore of the HSI was determined assuming 8μ diameter circular pores accumulated on a 150×150 square grid with 10μ spacing. These 22,500 pixels span a full width of roughly $30''$ and the grid was approximately centered on the determined image center. The number of pores with relative flux greater than or equal to f was plotted versus relative photon flux, f. It was found that this, the $\log N$-f curve, varied considerably depending on the exact relative positioning between the HSI pore grid and the simulated X-ray image, presumably due to the highly structured nature of the underlying image. In order to include this variation in our results, we ran 100 separate realizations varying the absolute center of the pore grid in 1μ steps in both the y- and z-direction. From

these 100 $\log N$-f curves were determined the mean curve, the mean plus and minus 1 σ curves, and the curves defining the minimum and maximum envelopes. These calculations were time-consuming and required a lot of disk space (about 50 Mb), so we only carried them out for the full HRMA models.

3.3. Use of Products

In most cases the use of a data product is obvious, however in some cases it is not. Below we describe the use of the HSI photon sampling $\log N$-f curve.

3.3.1. HSI photon sampling $\log N$-f curve

During XRCF calibration, the total count rate capability of the HSI will be limited by the desire to avoid count rate saturation in individual pores of the device. The $\log N$-f curve allows us to estimate the number of pores which would be saturated for a given total HSI count rate. Alternatively one can set limits on the total allowed HSI rate so that a certain limited number of pores would be saturated. Let us examine Fig. A.16. For simplicity we assume that saturation occurs at a rate, R_S, of 1 count s^{-1} $pore^{-1}$. Suppose that we wish to avoid saturating even a single pore. Then we read off the figure that the single brightest pore has a maximum relative photon flux, f, of $\sim$0.065. In order to avoid saturating this pore, the total HSI rate must be less than $R_S/f \sim 1/0.065 \sim 15\ s^{-1}$. If we allow the number of saturated pixels to be $\sim$10, then the total HSI rate can be larger: $R_S/f \sim 1/0.013 \sim 77\ s^{-1}$. This result depends sensitively on the detailed image morphology. For the off-axis case (Fig. A.32), one can avoid saturating any pore for a total count rate even as high as roughly $500\ s^{-1}$, assuming the same value of R_S as used above. Clearly we need to increase the fidelity of our HRMA model (by including mirror surface imperfections, alignment errors, etc.) before the $\log N$-f curve can be used confidently as a detailed planning tool for calibration observations. With this goal in mind, we also intend to produce $\log N$-f curves with parameters appropriate to the ACIS CCDs.

4. Simulation System

The philosophy we have embraced in the implementation of the software suite used to create the raytraces and perform the subsequent data analyses is to deconstruct the tasks required into simple atomic processes. Each process is then implemented as an individual C, FORTRAN, or `perl` program which communicates with other elements of the system via UNIX pipes. The photons appear as a stream of data, with each program acting as a filter (in the UNIX sense), working on one photon at a time, passing it along to the next program for further processing. The advantages of this approach are many. Modules can be inserted into the photon stream with ease, and development of new modules or changes to existing ones can be made without the fear of breaking other modules. The data interface is very simple and standard, which makes writing new modules straightforward. Additionally, there is no inherent limit to the number of photons that can be processed in such fashion, although individual analyses may run into limits (e.g., an iterative centering algorithm which must re-read the entire photon stream for each iteration).

At present we rely upon default system buffering to reduce the overhead of passing data through the system one ray at a time. Planned improvements include the use of shared memory to communicate between programs running on the same machine, as well as sockets to pass data between different machines. In this paradigm it is difficult to provide feedback from the end of the data stream to the beginning of the stream; we are investigating ways of providing this facility.

In order to tie the individual programs into a cohesive system, a "meta" language is required to choreograph them. This is usually accomplished on UNIX systems by using a "shell" program. A shell is a program which provides a convenient interface allowing a user to issue commands to the system and manipulate the administration of those commands and any output they may produce. Shells provide additional utility by implementing simple interpretive languages which users can use to automate tasks. We have chosen to use a utility, `perl`, which provides a much richer interface to the system and better process control than do the traditional shells. It differs from these as well in that it is relatively self-contained, providing the facilities of a large number of UNIX utilities. This eases multi-platform support

of our simulation system, as it provides a consistent level of support, independent of the vagaries of the underlying flavor of UNIX.

The suite of software used in this effort includes the following modules:

- a ray generator (`raygen`)
- aperture models simulating annular openings (`ap`)
- ray reflection (ray tracing) (SAOsac)
- spatial distortion (e.g., Gaussian detector spatial response) (`blur`)
- spatial binning (`spatquant`)
- center detection and annular binning of the photons (`radprof`)
- pinhole scan simulator (`pinhole`)
- various other support routines
    - compile encircled energies for particular apertures and generate TEX, LATEX, TEXsis, and straight `ASCII` tables (`enen-ap`)
    - convert binned photons to PSF's and encircled energy curves (`prof2enen`, `profnorm`)
    - grayscale plots (`imageplot`)

These are tied together in various guises by `perl` programs to form particular tasks. Fig. 4.1 presents an overview of the system; a more detailed description follows.

The top level `perl` scripts used are as follows:

`pipe-plex`

`pipe-plex` is the highest level script and determines the source of rays to be processed (either from a file or from the ray generator), merges the individual shells into a full HRMA, if necessary, and sends the photons for processing to `hdbk-process`.

`hdbk-process`

this script acts as a dispatcher for the rays passed to it by `pipe-plex`, directing them in turn to a suite of analysis scripts.

`psfenen`

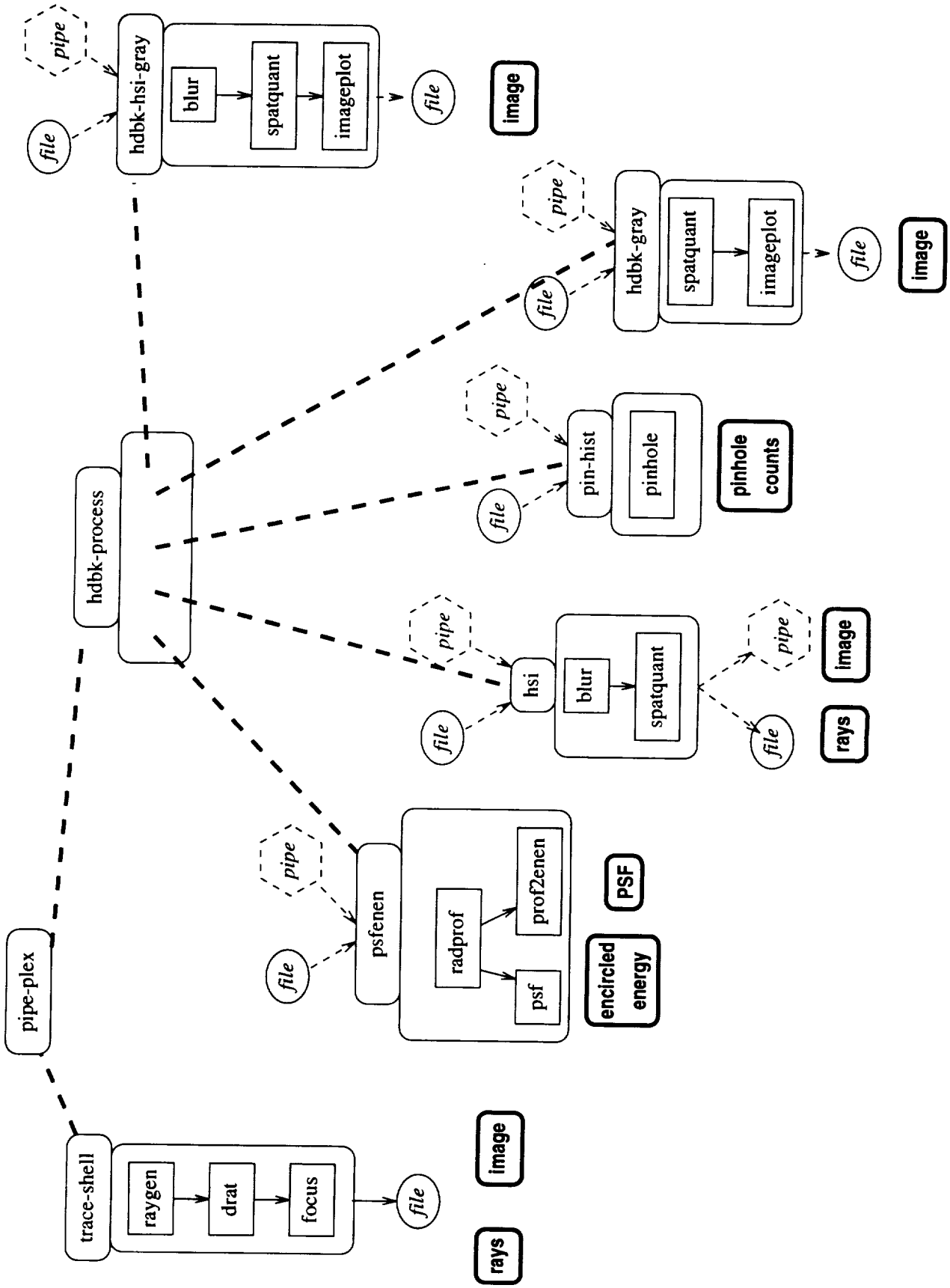

Figure 4.1: A graphical representation of the simulation software.

this script takes a stream of photons, determines the center of the photon distribution at a focal position, and generates azimuthally averaged PSF and encircled energy distributions.

`pin-hist`

this script passes the photons through a grid of circular apertures, simulating pinhole flux measurements at the focal plane

`hdbk-gray`

this generates grayscale images of the photon distribution at a particular focal plane.

`hdbk-hsi-gray`

this generates grayscale images of the photon distribution at a particular focal plane as seen by a simulated HSI.

There are several other subsidiary scripts (for example, the HSI model is a script which ties together a Gaussian blurring program and a spatial quantizing program) that perform analyses, as well as generating the input files for the plotting programs used to generate the graphical representation of the data. Each of these scripts or programs may be used outside of the hierarchy, as well.

It is imperative that all of the particulars of a data product be stored so that different tasks can manipulate it without requiring the human operator to act as a communications bridge between them. As each analysis is completed, its particulars are stored in a database, minimizing to a great extent transcription errors.

5. References

Glenn, P., & Noll, R. 1982, "Optical Surface Analysis Code," Perkin Elmer final report for NASA Contract NAS5-25802.

Henke, B. L., Gullikson, E. M., & Davis, J. C. 1993, *Atomic Data and Nuclear Data Tables*, **54:2**, 181.

Hughes, J. P., & Podgorski, W. 1990, "X-Ray Alignment of the VETA-I and Studies of the VETA-I FWHM Measurements," SAO-AXAF-90-040.

Van Speybroeck, L. 1989, SAO memorandum to J. Humphreys entitled "Mirror Prescription" (20 October 1989).

Zhao, P., Freeman, M. D., Jerius, D., & Shao. Y. 1994, "AXAF VETA-I Mirror Ring Focus Measurements," presented at the 1993 SPIE annual San Diego meeting, in press.

A. Data Products

Table A.1 presents the positions of the centers and centroids of the simulations. In this case center refers to the iterative clipping method, and centroid is the center of weight.

Data for each combination of simulation parameters (as outlined in Table 2.4) are presented in the following tables and figures. Data sets are presented in the order MP1, MP3, MP4, MP6, HRMA, comprising the following products:

1. A logarithmically scaled focal plane image. This is binned at 1 μ for on-axis images, 10 μ for off-axis images.
2. A logarithmically scaled focal plane image as seen by the HSI.
3. A fractional encircled energy diagram. Four curves are plotted, for the different shifted centers. The centers are indicated on the plot.
4. For the complete HRMA only: HSI photon sampling $\log N$-f curves showing the number of 8 μ pores with flux greater than (or equal to) f versus the relative photon flux, f. Five curves, summarizing the 100 realizations, are shown. The left- and right-most curves are the minimum and maximum envelopes, the middle curve is the mean and the dashed curves are the mean plus and minus 1 σ curves.

Summary tables are presented after the data for HRMA:

1. A table of encircled energy fractions at interesting radii. The focal positions for each MP is presented at the top of the table.

Table A.1: Simulation Characteristics

Model	Energy	Elevation	Azimuth	Shell	Focus	Centroid		Center	
	(keV)	(′)	(′)		(mm)	y (mm)	z (mm)	y (mm)	z (mm)
xrcf	0.277	0.0	0.0	1	11130.9	−0.0000	−0.0233	−0.0000	−0.0234
xrcf	0.277	0.0	0.0	3	11131.0	−0.0000	−0.0251	−0.0000	−0.0251
xrcf	0.277	0.0	0.0	4	11131.1	+0.0000	−0.0247	+0.0000	−0.0247
xrcf	0.277	0.0	0.0	6	11131.2	−0.0000	−0.0263	−0.0000	−0.0263
xrcf	0.277	0.0	0.0	HRMA	11131.0	−0.0000	−0.0245	−0.0000	−0.0245
xrcf	0.277	15.0	0.0	1	11121.7	+0.0001	+44.5041	+0.0001	+44.5041
xrcf	0.277	15.0	0.0	3	11117.3	−0.0001	+44.4907	−0.0001	+44.4909
xrcf	0.277	15.0	0.0	4	11113.7	+0.0003	+44.4818	+0.0003	+44.4820
xrcf	0.277	15.0	0.0	6	11100.6	+0.0006	+44.4388	+0.0006	+44.4389
xrcf	0.277	15.0	0.0	HRMA	11118.6	+0.0000	+44.4999	+0.0000	+44.4999

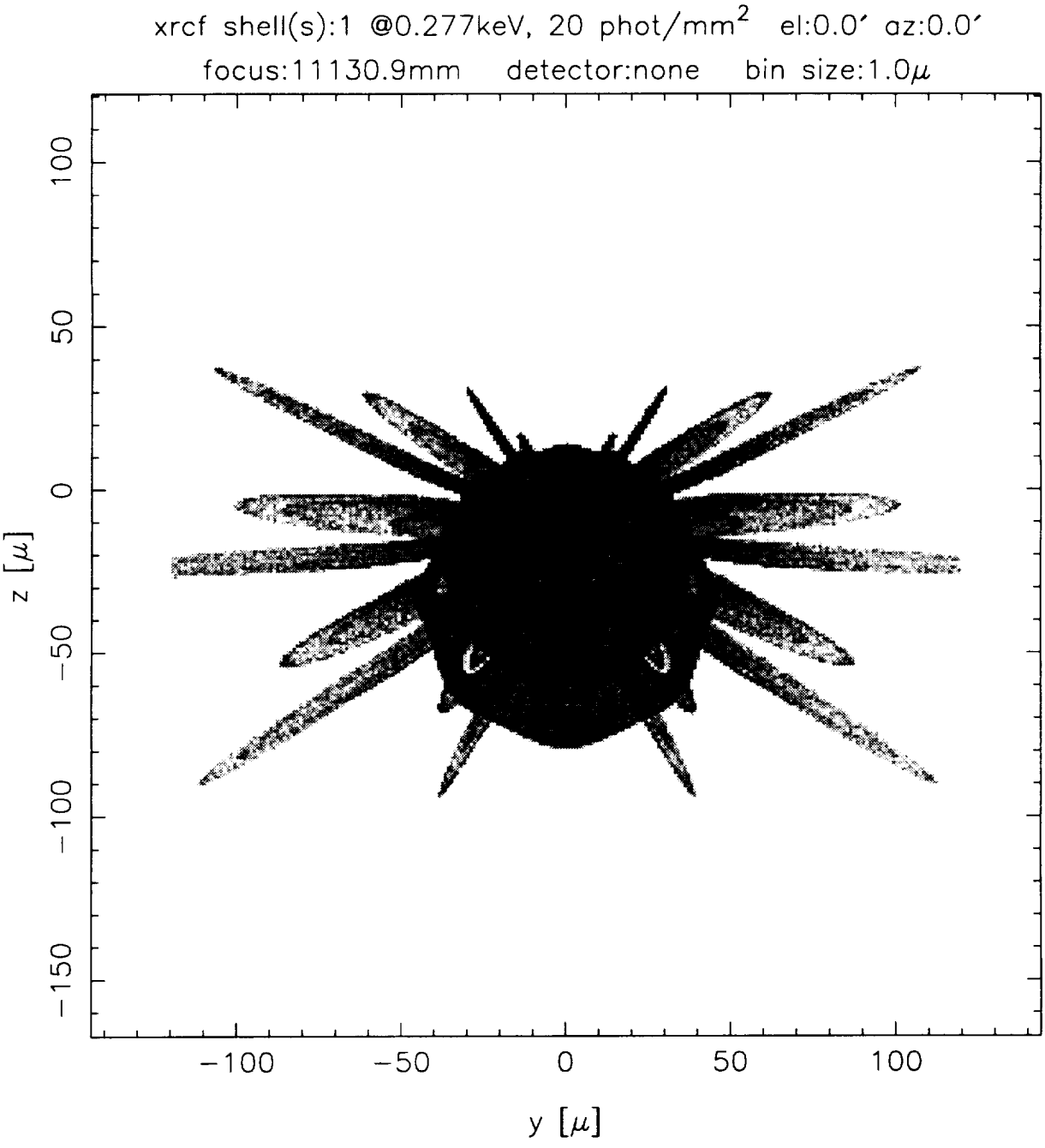
xrcf shell(s):1 @0.277keV, 20 phot/mm^2 el:0.0′ az:0.0′
focus:11130.9mm detector:none bin size:1.0μ
z [μ]
100
50
0
−50
−100
−150
−100
−50
0
50
100
y [μ]

Figure A.1:

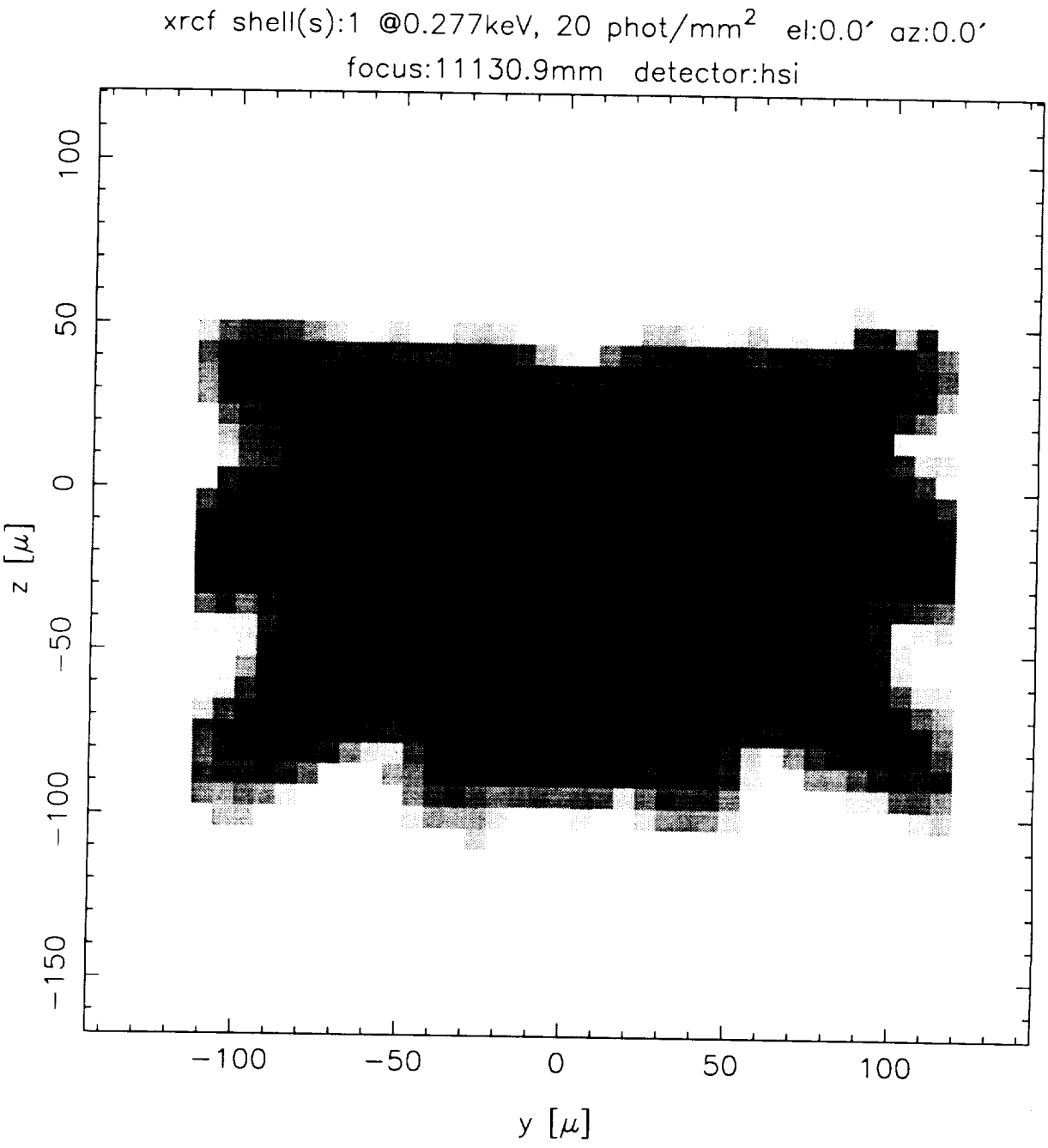
xrcf shell(s):1 @0.277keV, 20 phot/mm^2 el:0.0′ az:0.0′
focus:11130.9mm detector:hsi
z [μ]
y [μ]
100
50
0
−50
−100
−150
−100
−50
0
50
100

Figure A.2:

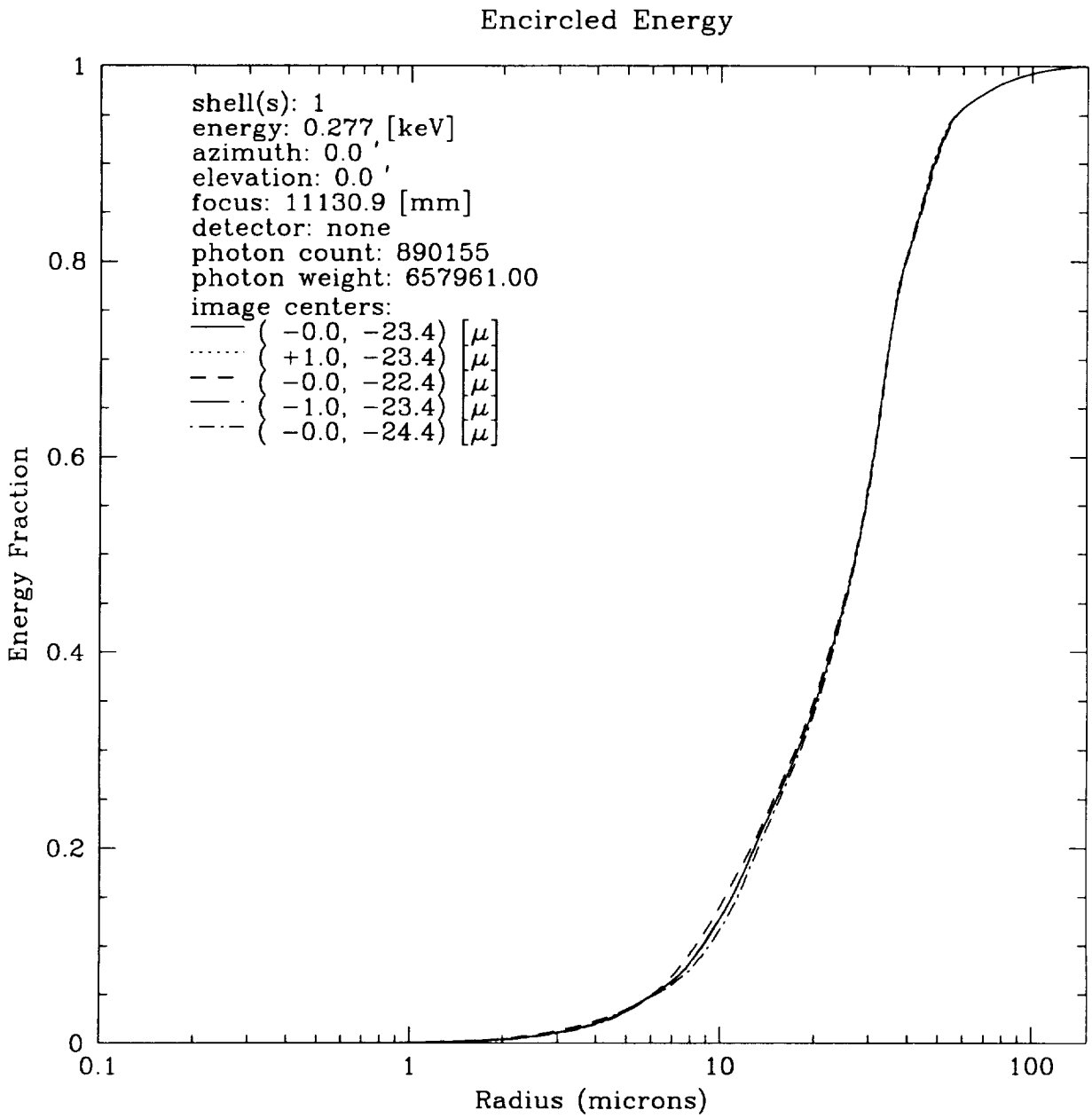
Encircled Energy
shell(s): 1
energy: 0.277 [keV]
azimuth: 0.0 '
elevation: 0.0 '
focus: 11130.9 [mm]
detector: none
photon count: 890155
photon weight: 657961.00
image centers:
(−0.0, −23.4) [μ]
(+1.0, −23.4) [μ]
(−0.0, −22.4) [μ]
(−1.0, −23.4) [μ]
(−0.0, −24.4) [μ]
Energy Fraction
0
0.2
0.4
0.6
0.8
1
0.1
1
10
100
Radius (microns)

Figure A.3:

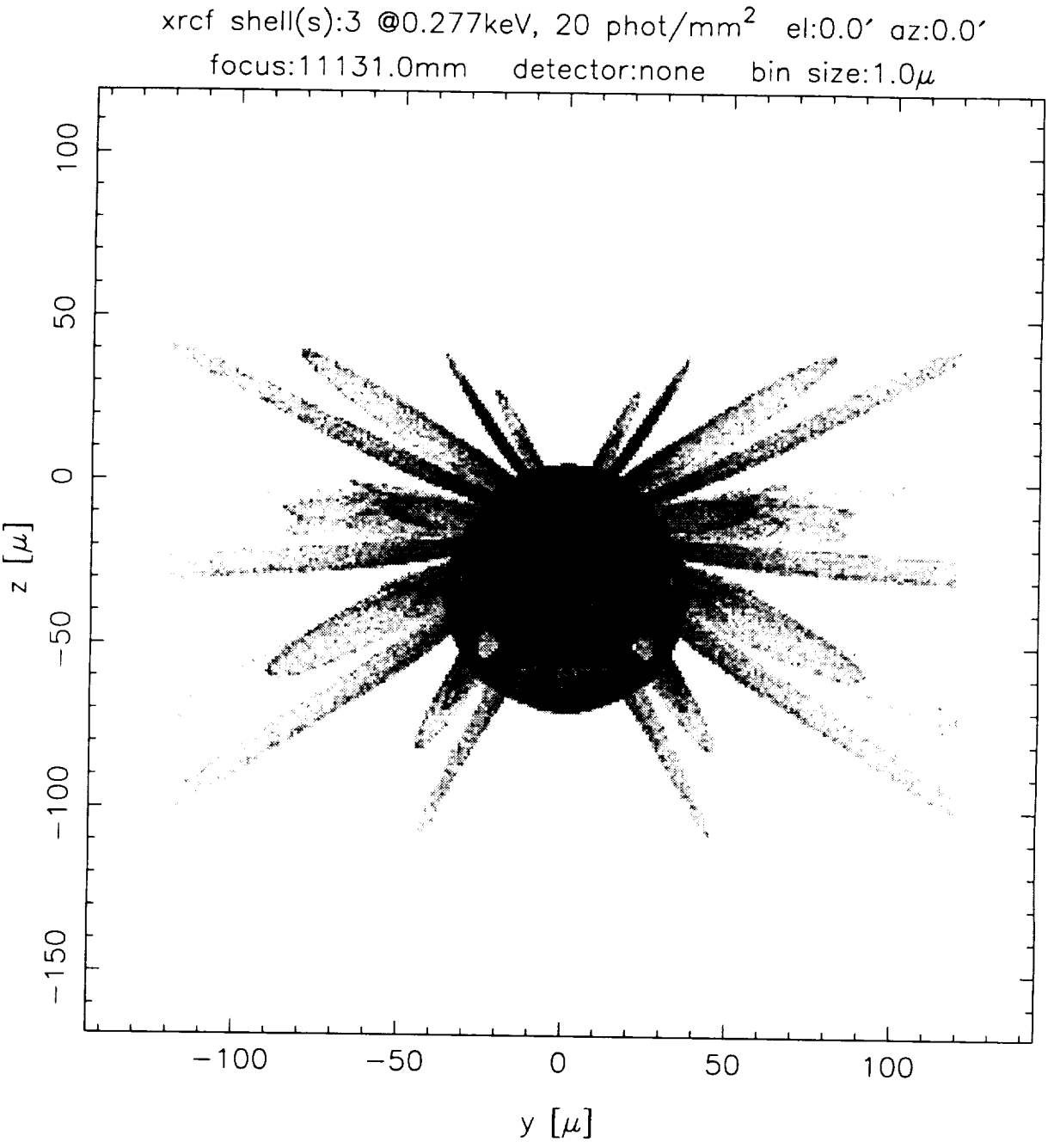
xrcf shell(s):3 @0.277keV, 20 phot/mm^2 el:0.0′ az:0.0′
focus:11131.0mm detector:none bin size:1.0μ
z [μ]
100
50
0
−50
−100
−150
−100
−50
0
50
100
y [μ]

Figure A.4:

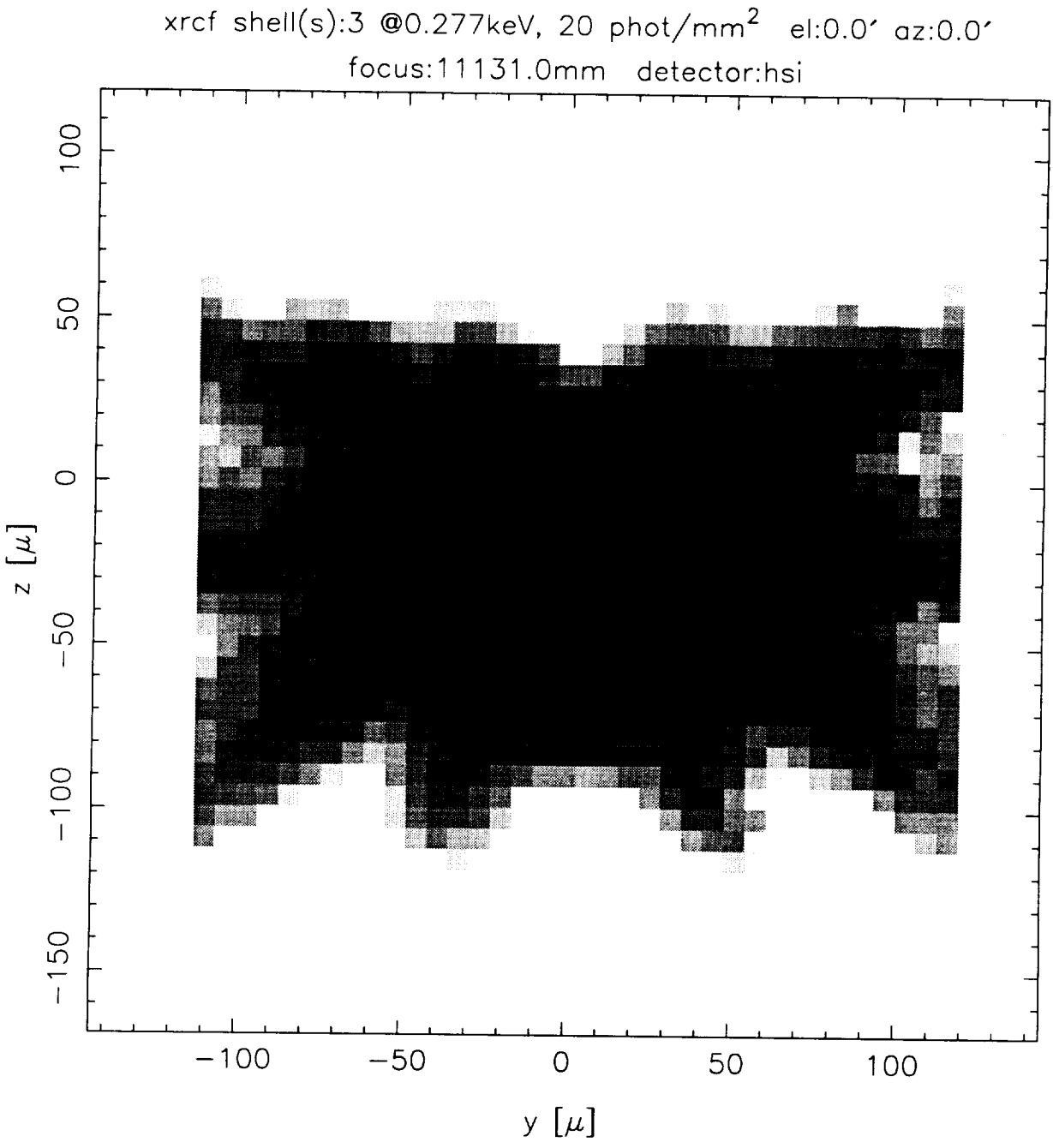
xrcf shell(s):3 @0.277keV, 20 phot/mm^2 el:0.0′ az:0.0′
focus:11131.0mm detector:hsi
z [μ]
y [μ]
100
50
0
−50
−100
−150
−100
−50
0
50
100

Figure A.5:

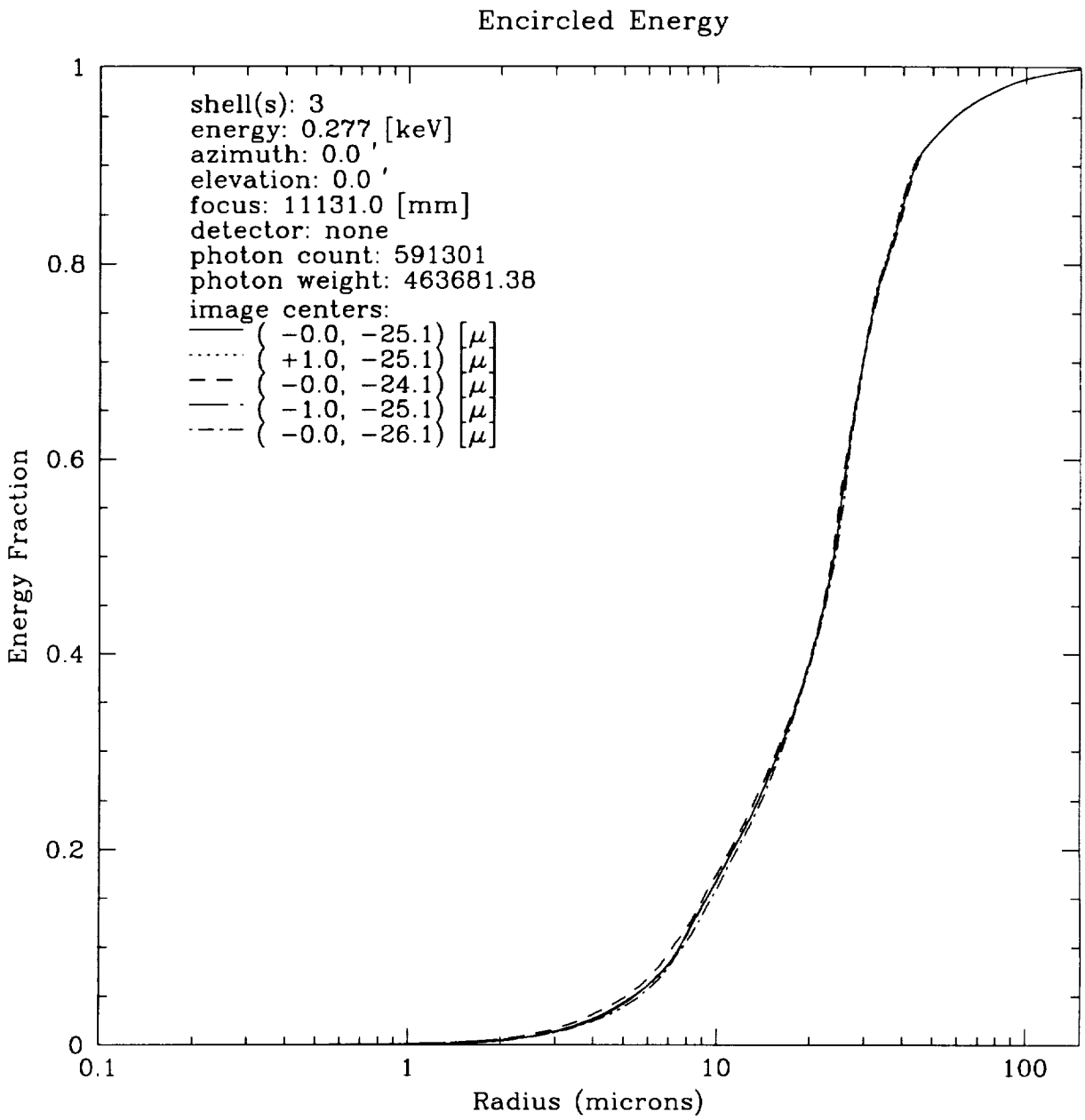
Encircled Energy
shell(s): 3
energy: 0.277 [keV]
azimuth: 0.0 '
elevation: 0.0 '
focus: 11131.0 [mm]
detector: none
photon count: 591301
photon weight: 463681.38
image centers:
(-0.0, -25.1) [μ]
(+1.0, -25.1) [μ]
(-0.0, -24.1) [μ]
(-1.0, -25.1) [μ]
(-0.0, -26.1) [μ]
Energy Fraction
0
0.2
0.4
0.6
0.8
1
0.1
1
10
100
Radius (microns)

Figure A.6:

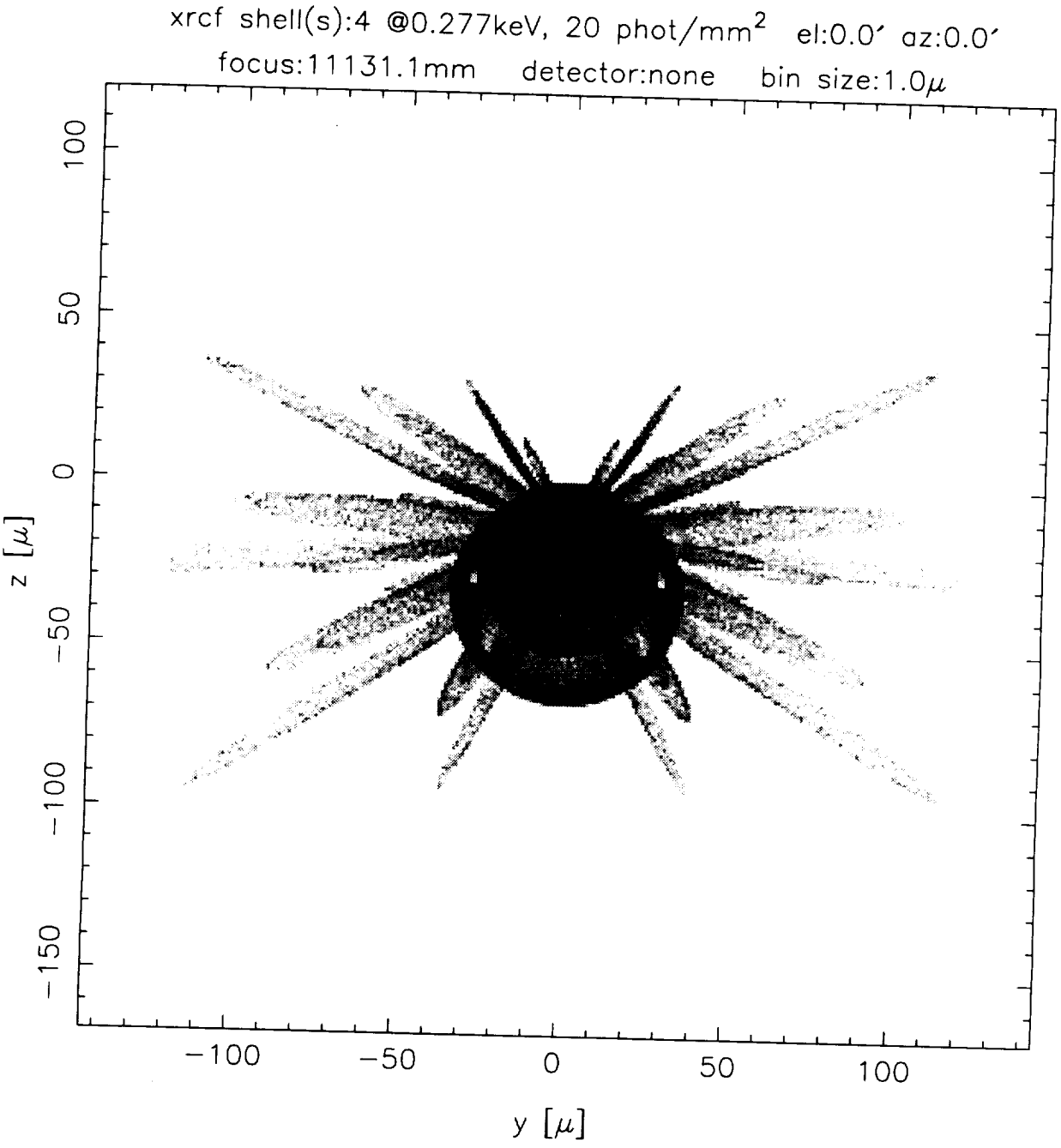
xrcf shell(s):4 @0.277keV, 20 phot/mm^2 el:0.0′ az:0.0′
focus:11131.1mm detector:none bin size:1.0μ
z [μ]
y [μ]
100
50
0
−50
−100
−150
−100
−50
0
50
100

Figure A.7:

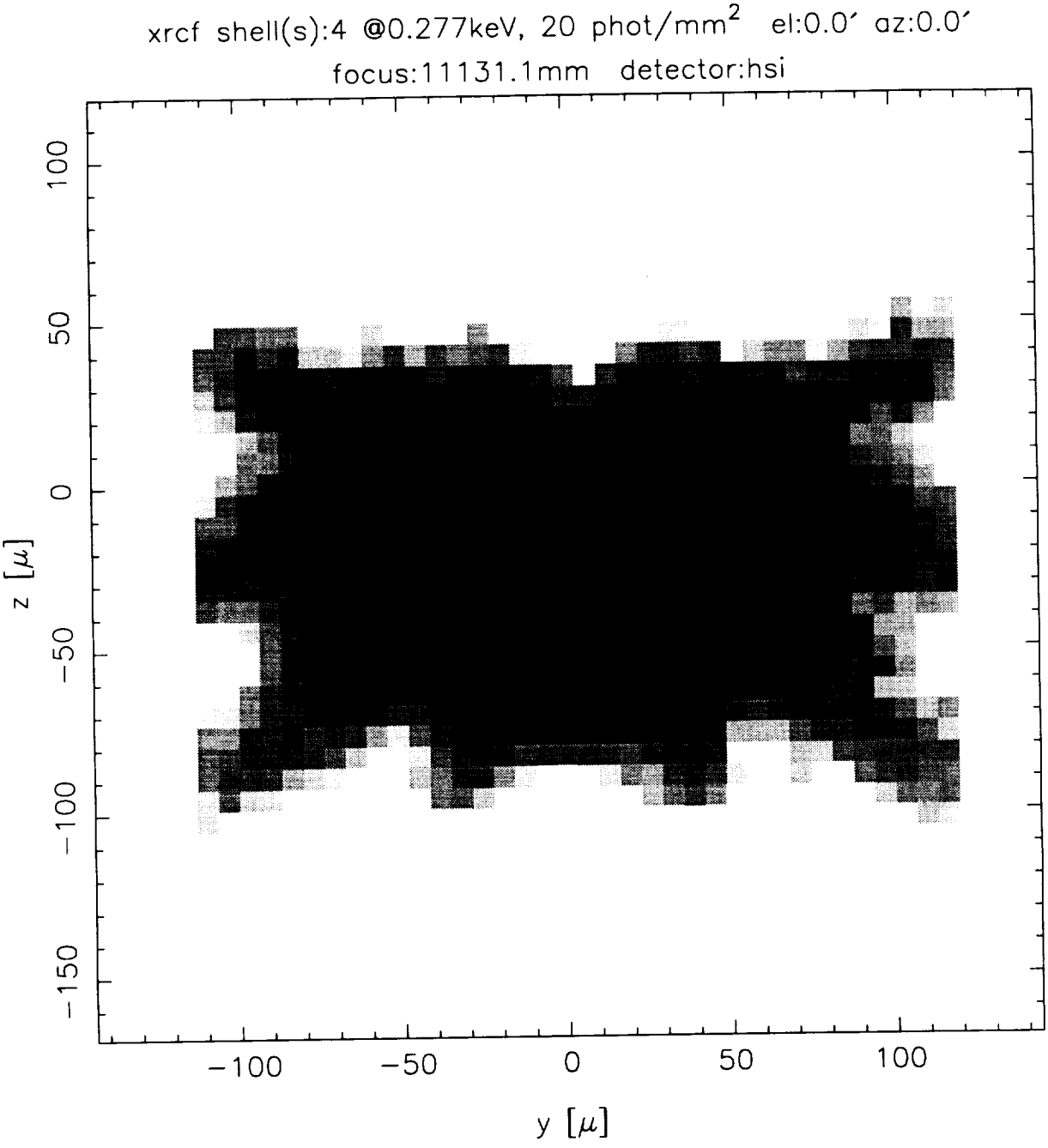
xrcf shell(s):4 @0.277keV, 20 phot/mm^2 el:0.0′ az:0.0′
focus:11131.1mm detector:hsi
z [μ]
100
50
0
−50
−100
−150
−100
−50
0
50
100
y [μ]

Figure A.8:

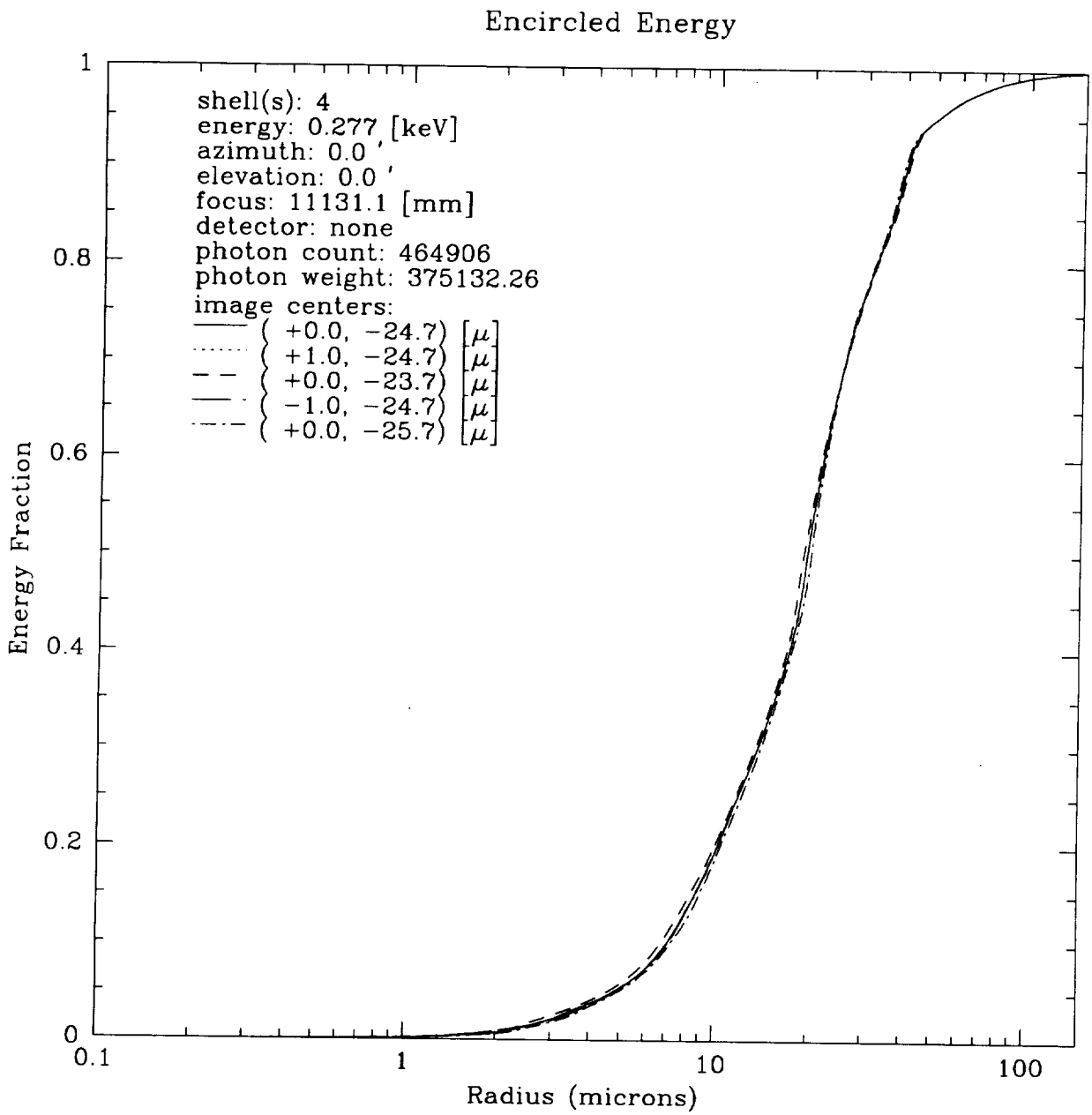
Encircled Energy
shell(s): 4
energy: 0.277 [keV]
azimuth: 0.0 '
elevation: 0.0 '
focus: 11131.1 [mm]
detector: none
photon count: 464906
photon weight: 375132.26
image centers:
(+0.0, −24.7) [μ]
(+1.0, −24.7) [μ]
(+0.0, −23.7) [μ]
(−1.0, −24.7) [μ]
(+0.0, −25.7) [μ]
Energy Fraction
0
0.2
0.4
0.6
0.8
1
0.1
1
10
100
Radius (microns)

Figure A.9:

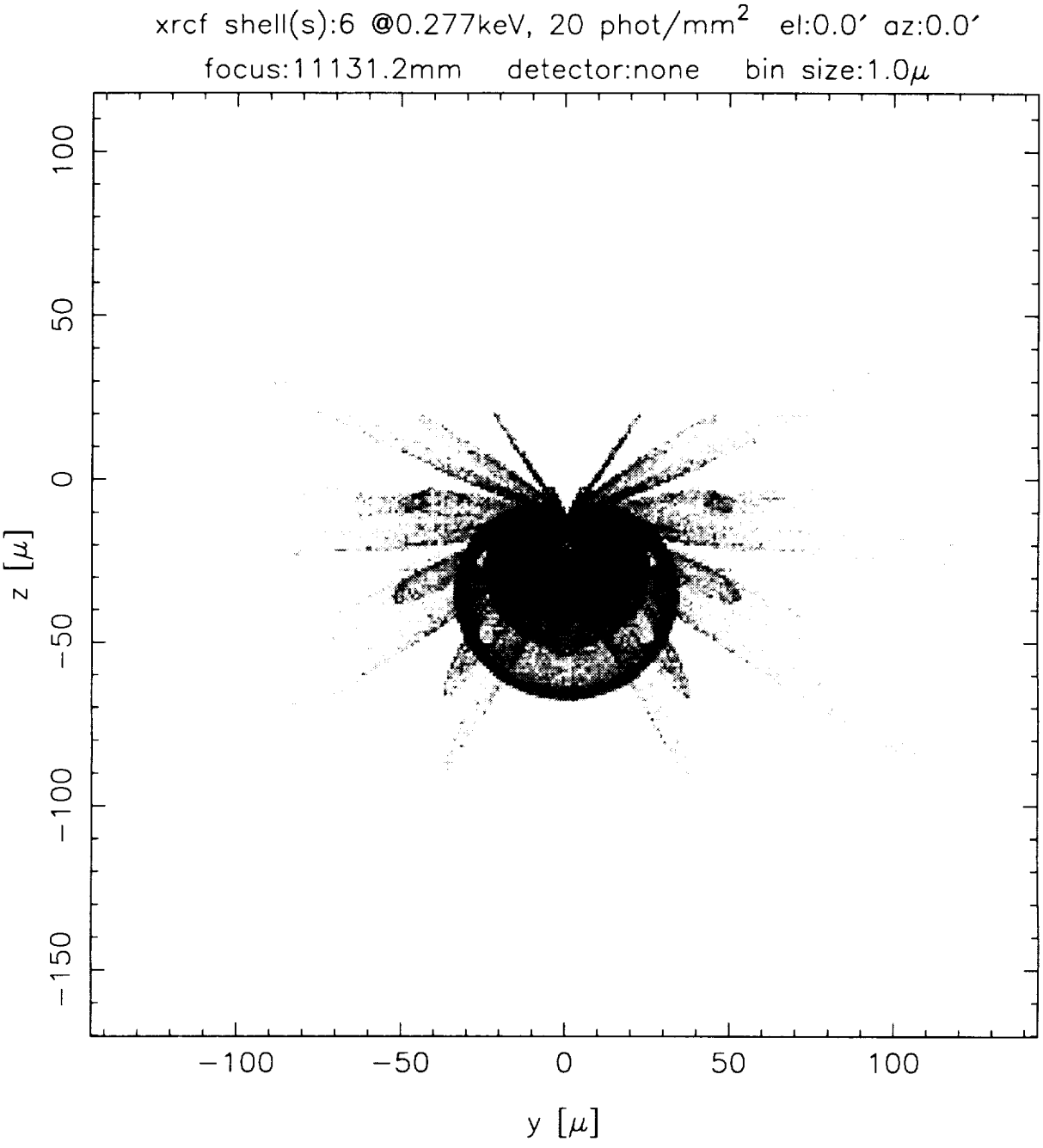
xrcf shell(s):6 @0.277keV, 20 phot/mm^2 el:0.0′ az:0.0′
focus:11131.2mm detector:none bin size:1.0μ
z [μ]
y [μ]
100
50
0
−50
−100
−150
−100
−50
0
50
100

Figure A.10:

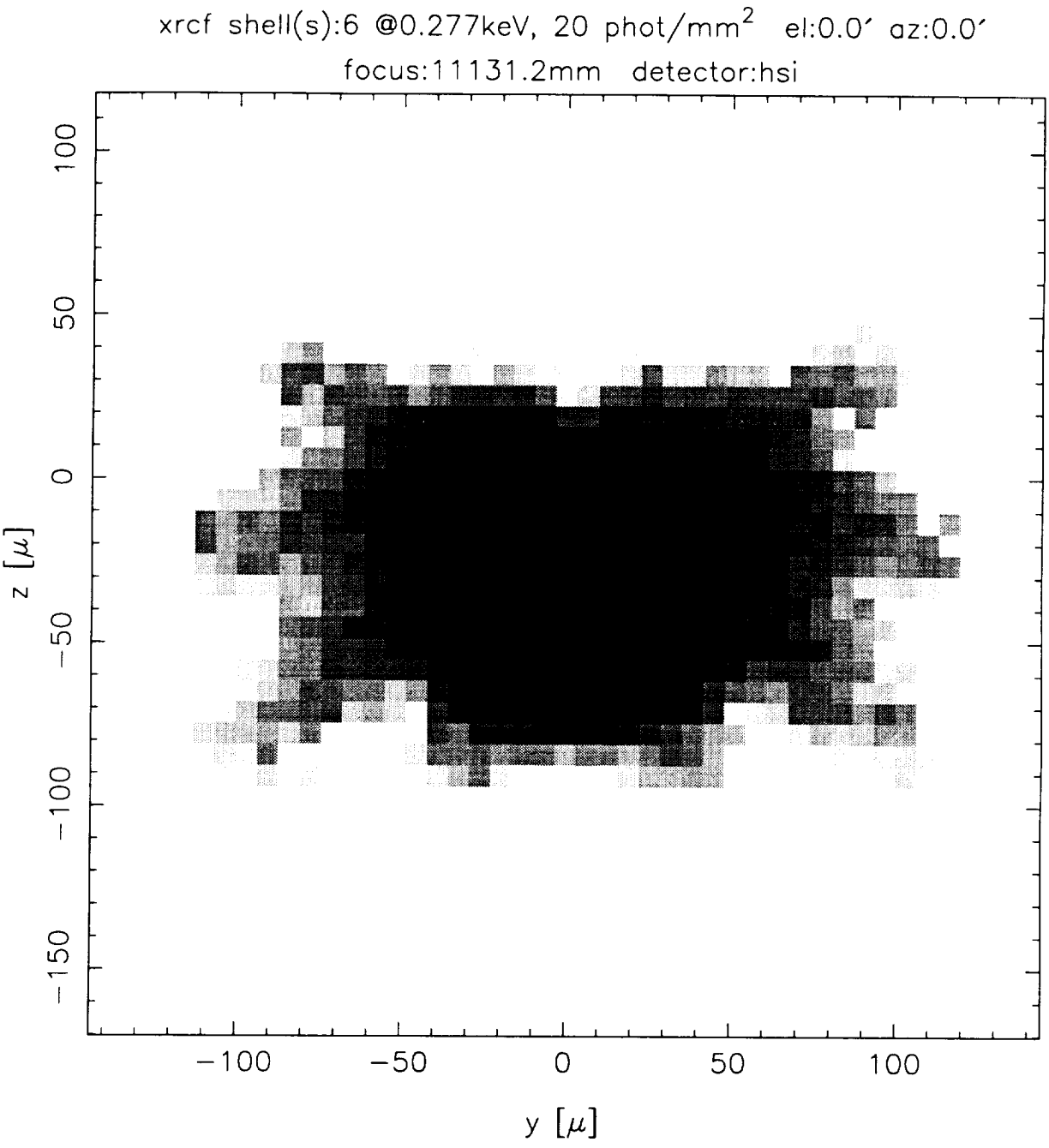
xrcf shell(s):6 @0.277keV, 20 phot/mm^2 el:0.0′ az:0.0′
focus:11131.2mm detector:hsi
z [μ]
y [μ]
100
50
0
−50
−100
−150
−100
−50
0
50
100

Figure A.11:

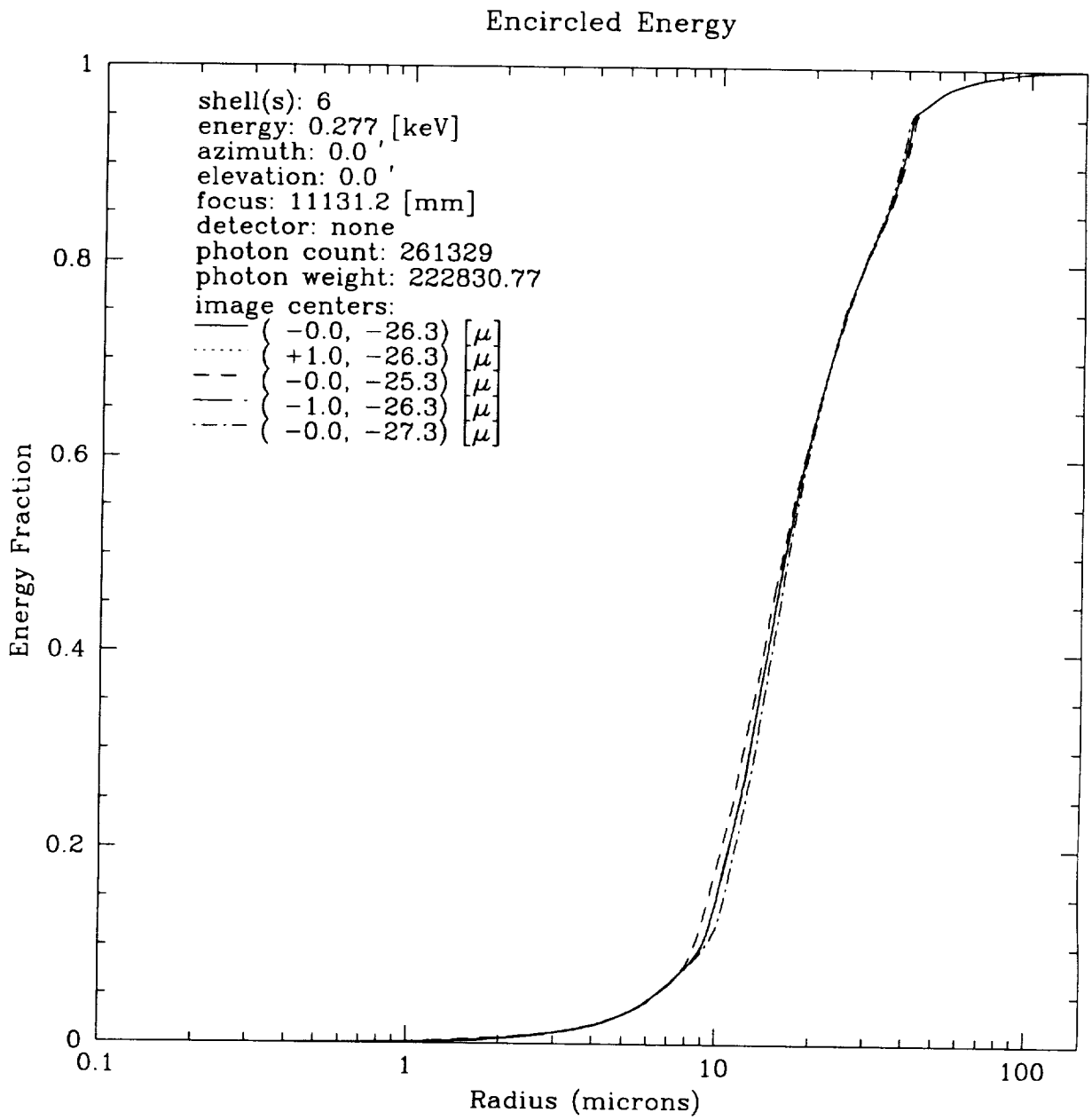
Encircled Energy
shell(s): 6
energy: 0.277 [keV]
azimuth: 0.0 '
elevation: 0.0 '
focus: 11131.2 [mm]
detector: none
photon count: 261329
photon weight: 222830.77
image centers:
(−0.0, −26.3) [μ]
(+1.0, −26.3) [μ]
(−0.0, −25.3) [μ]
(−1.0, −26.3) [μ]
(−0.0, −27.3) [μ]
Energy Fraction
0
0.2
0.4
0.6
0.8
1
0.1
1
10
100
Radius (microns)

Figure A.12:

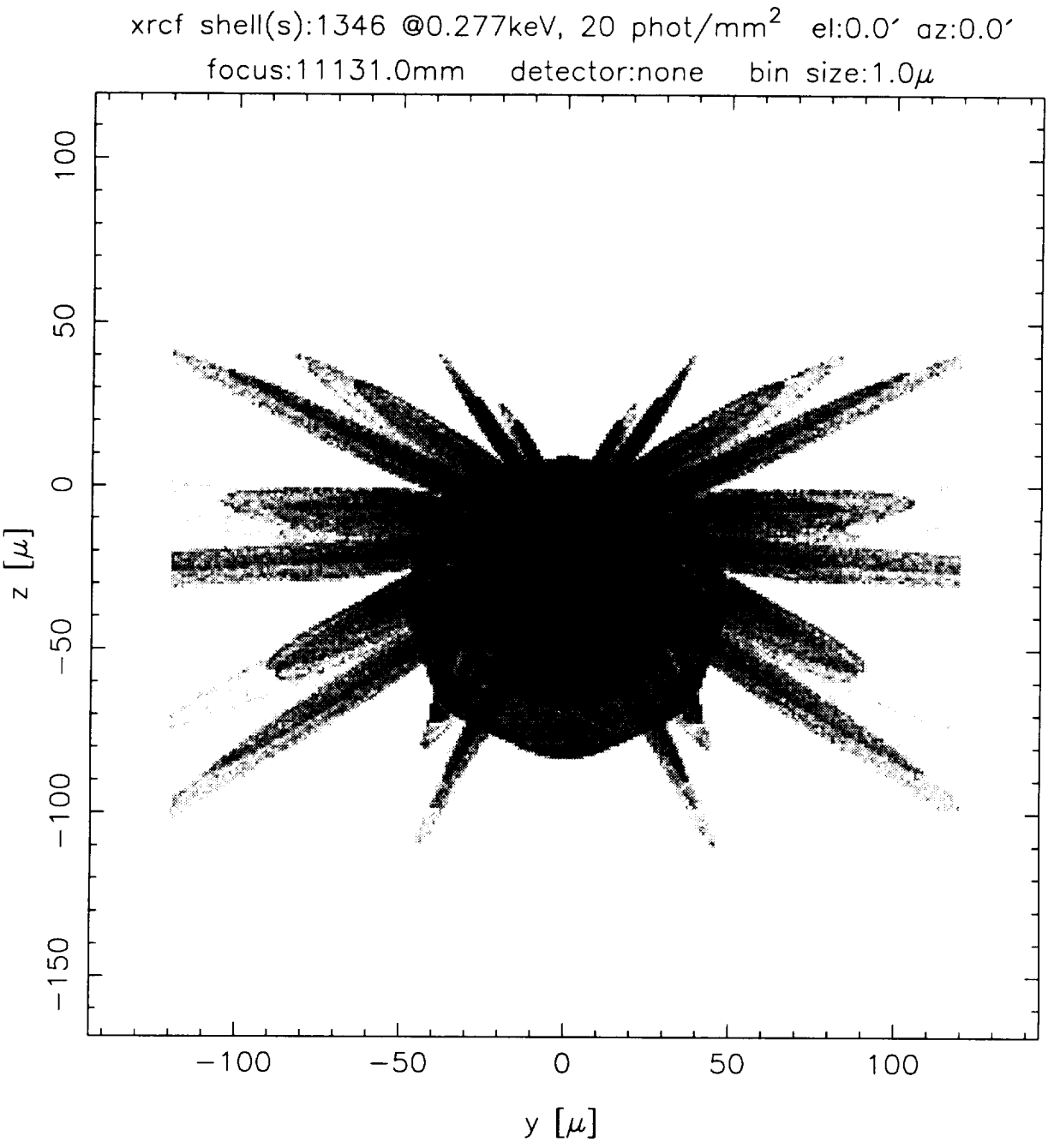
xrcf shell(s):1346 @0.277keV, 20 phot/mm^2 el:0.0′ az:0.0′
focus:11131.0mm detector:none bin size:1.0μ
z [μ]
y [μ]
100
50
0
−50
−100
−150
−100
−50
0
50
100

Figure A.13:

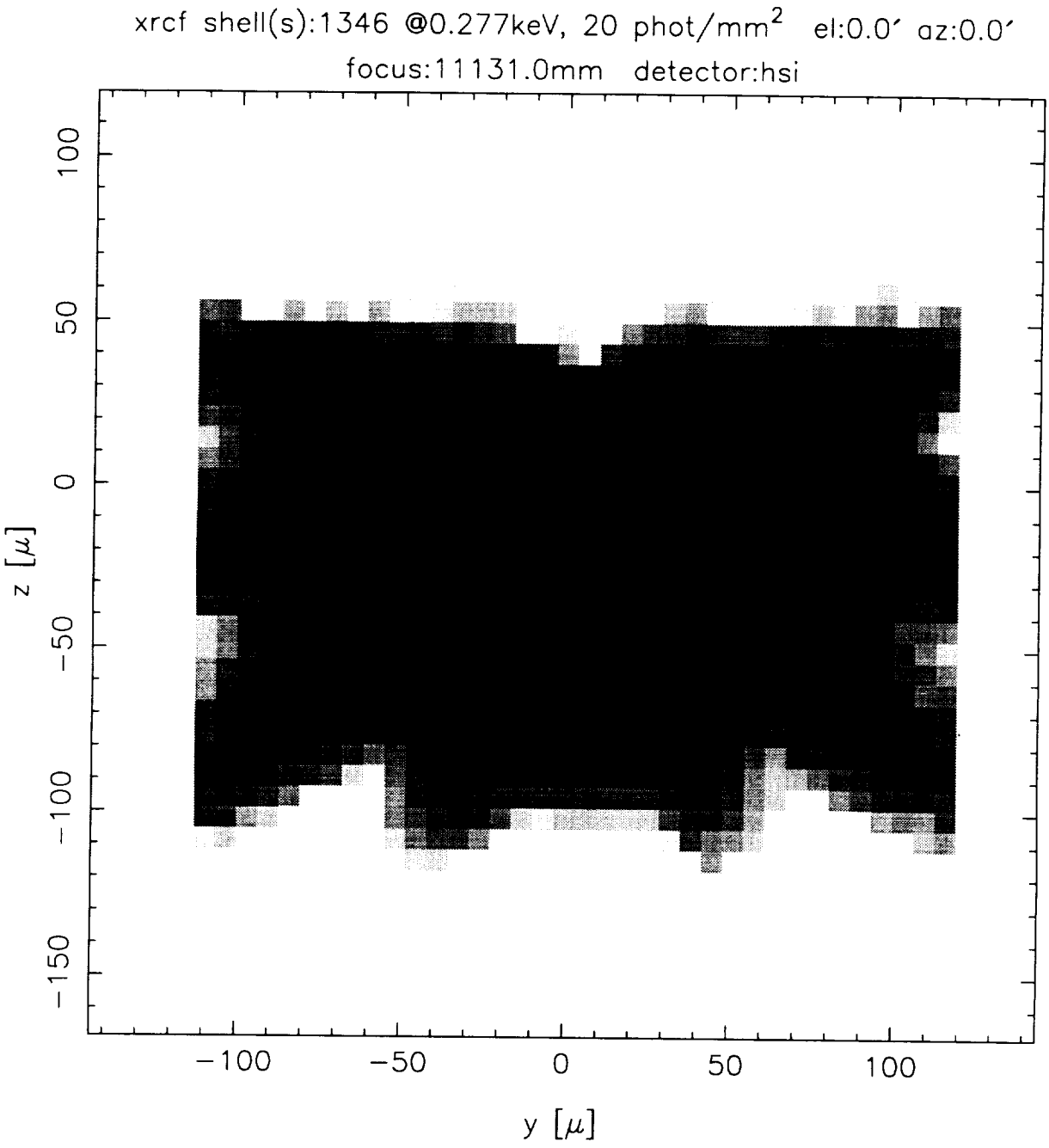
xrcf shell(s):1346 @0.277keV, 20 phot/mm^2 el:0.0′ az:0.0′
focus:11131.0mm detector:hsi
z [μ]
y [μ]
100
50
0
−50
−100
−150
−100
−50
0
50
100

Figure A.14:

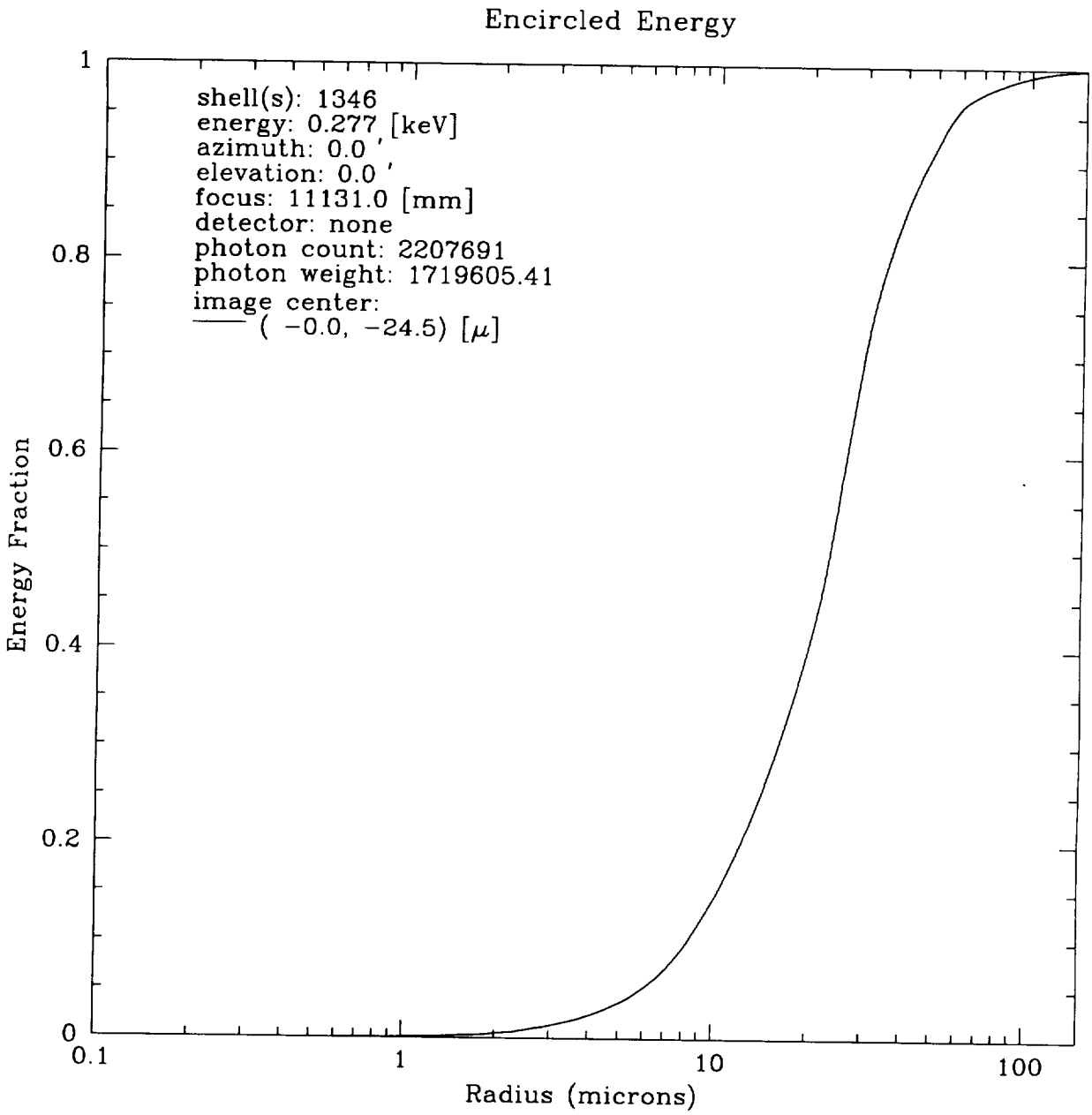
Encircled Energy
shell(s): 1346
energy: 0.277 [keV]
azimuth: 0.0 '
elevation: 0.0 '
focus: 11131.0 [mm]
detector: none
photon count: 2207691
photon weight: 1719605.41
image center:
(-0.0, -24.5) [μ]
Energy Fraction
Radius (microns)
0
0.2
0.4
0.6
0.8
1
0.1
1
10
100

Figure A.15:

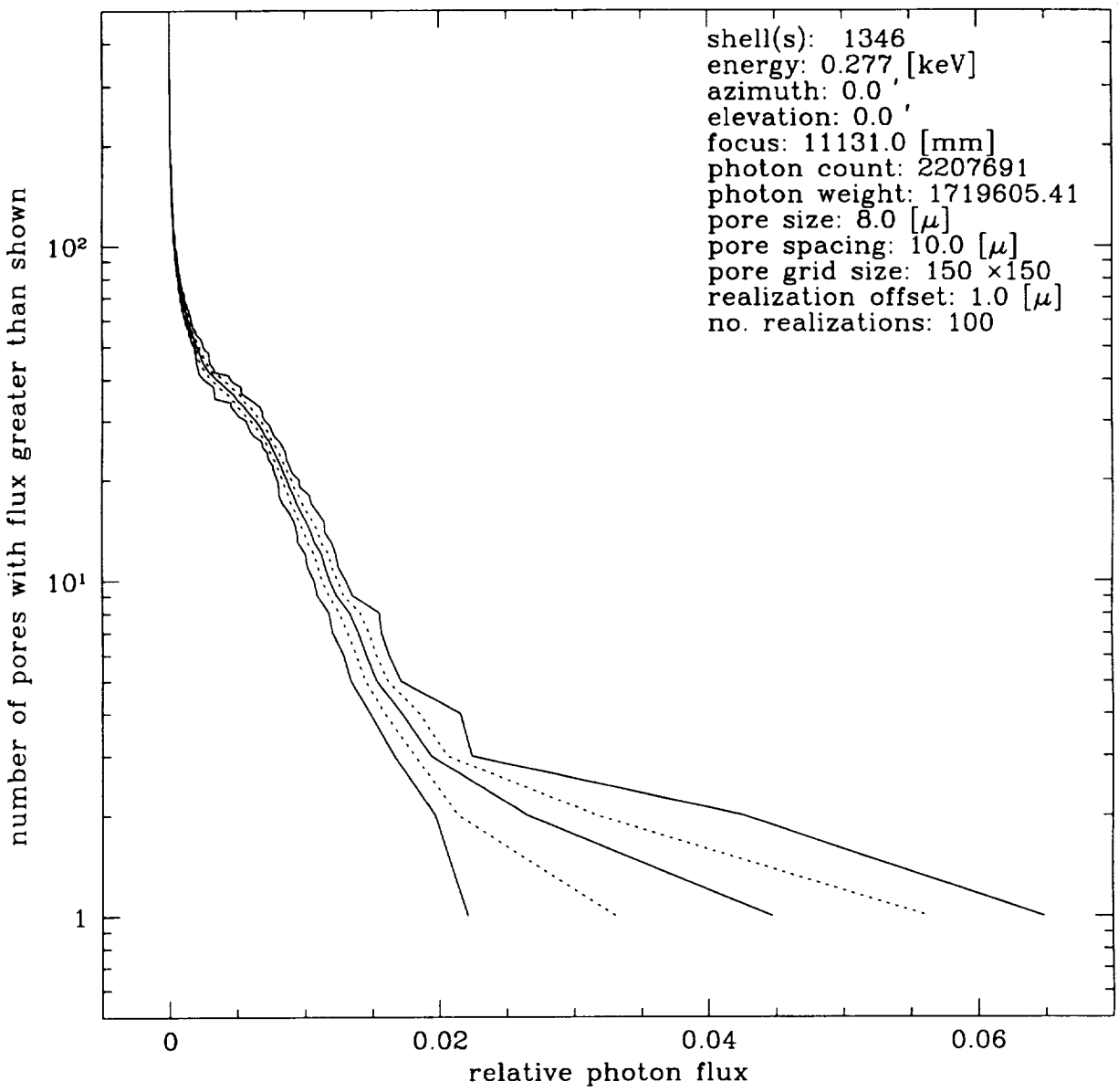
shell(s): 1346
energy: 0.277 [keV]
azimuth: 0.0 '
elevation: 0.0 '
focus: 11131.0 [mm]
photon count: 2207691
photon weight: 1719605.41
pore size: 8.0 [μ]
pore spacing: 10.0 [μ]
pore grid size: 150 ×150
realization offset: 1.0 [μ]
no. realizations: 100
number of pores with flux greater than shown
10²
10¹
1
0
0.02
0.04
0.06
relative photon flux

Figure A.16:

Table A.2: Encircled energy fractions for:
xrcf @ 0.277KeV; Azimuth: 0.00′, Elevation: 0.00′

radius (mm) (focus (mm))	shell 1 (11130.9)	shell 3 (11131.0)	shell 4 (11131.1)	shell 6 (11131.2)	HRMA (11131.0)
0.005	0.03333	0.04341	0.05383	0.02941	0.03636
0.010	0.12797	0.16785	0.19021	0.14314	0.14158
0.015	0.24560	0.27945	0.33260	0.42522	0.27135
0.020	0.34262	0.39066	0.51553	0.62833	0.40199
0.025	0.44806	0.54148	0.68377	0.74195	0.55937
0.030	0.56922	0.70775	0.77405	0.81039	0.71006
0.035	0.71907	0.79929	0.83484	0.86089	0.79858
0.040	0.80757	0.86228	0.90212	0.92531	0.85304
0.045	0.86336	0.90960	0.93943	0.96209	0.89145
0.050	0.91267	0.92762	0.95200	0.97310	0.92003
0.060	0.95772	0.95251	0.96994	0.98497	0.96106
0.070	0.97224	0.96689	0.98024	0.99064	0.97480
0.080	0.98254	0.97610	0.98732	0.99400	0.98279
0.090	0.98880	0.98338	0.99126	0.99636	0.98856
0.100	0.99286	0.98820	0.99435	0.99769	0.99246
0.150	0.99992	0.99828	0.99969	0.99997	0.99946
0.200	1.00000	1.00000	1.00000	1.00000	1.00000

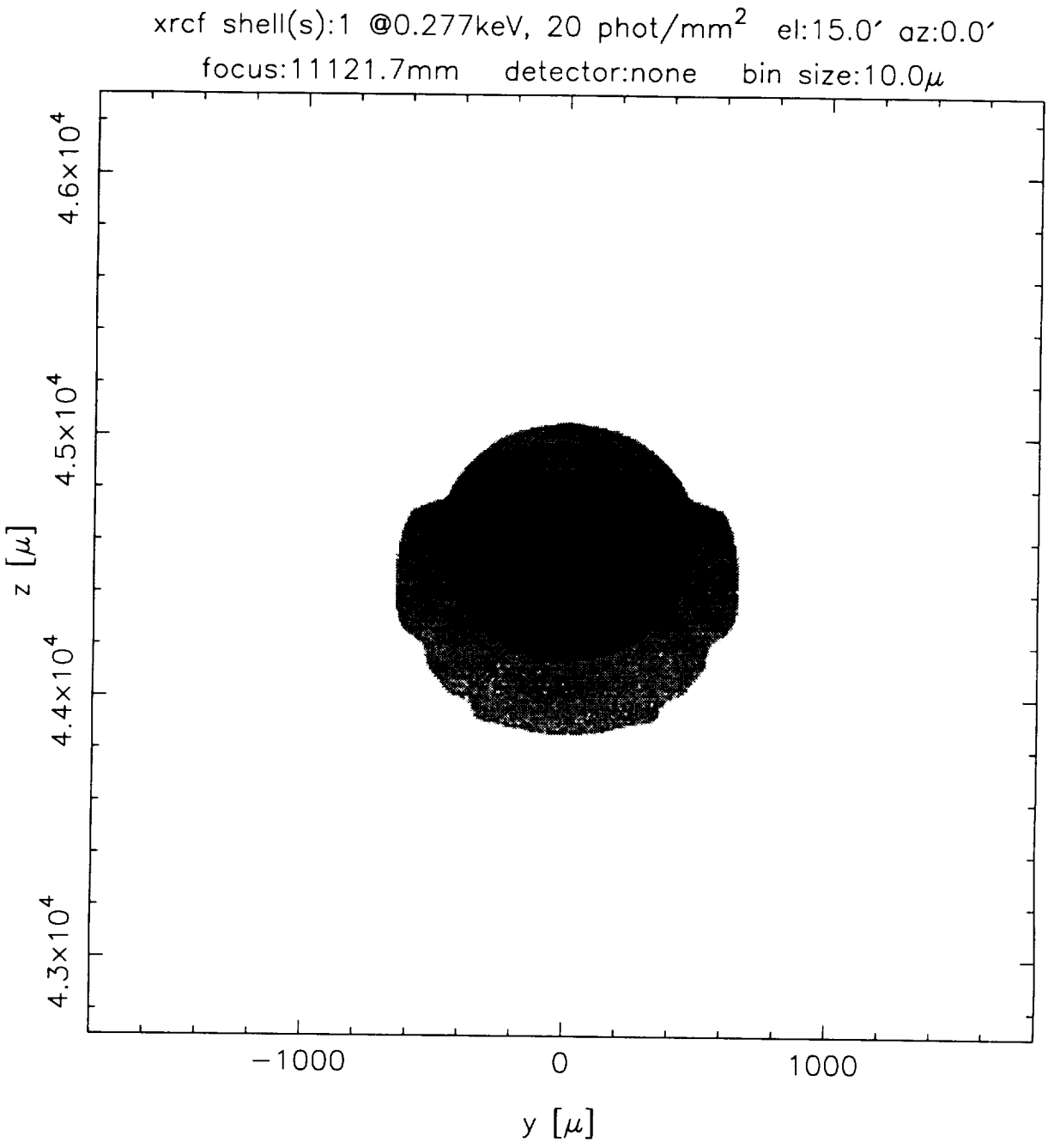
xrcf shell(s):1 @0.277keV, 20 phot/mm^2 el:15.0′ az:0.0′
focus:11121.7mm detector:none bin size:10.0μ
4.6×10^4
4.5×10^4
4.4×10^4
4.3×10^4
z [μ]
−1000
0
1000
y [μ]

Figure A.17:

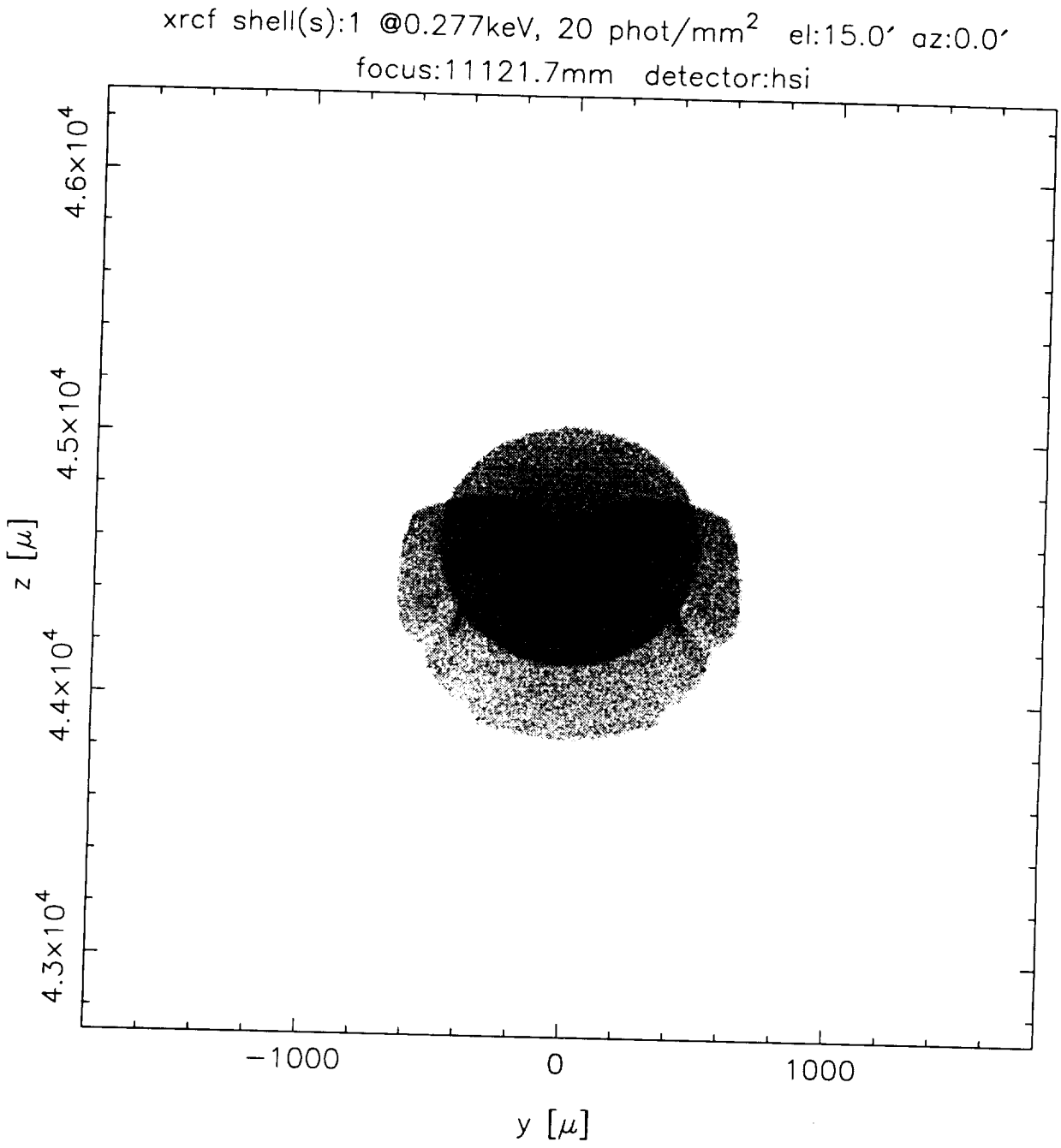
xrcf shell(s):1 @0.277keV, 20 phot/mm^2 el:15.0′ az:0.0′
focus:11121.7mm detector:hsi
4.6×10^4
4.5×10^4
4.4×10^4
4.3×10^4
z [μ]
−1000
0
1000
y [μ]

Figure A.18:

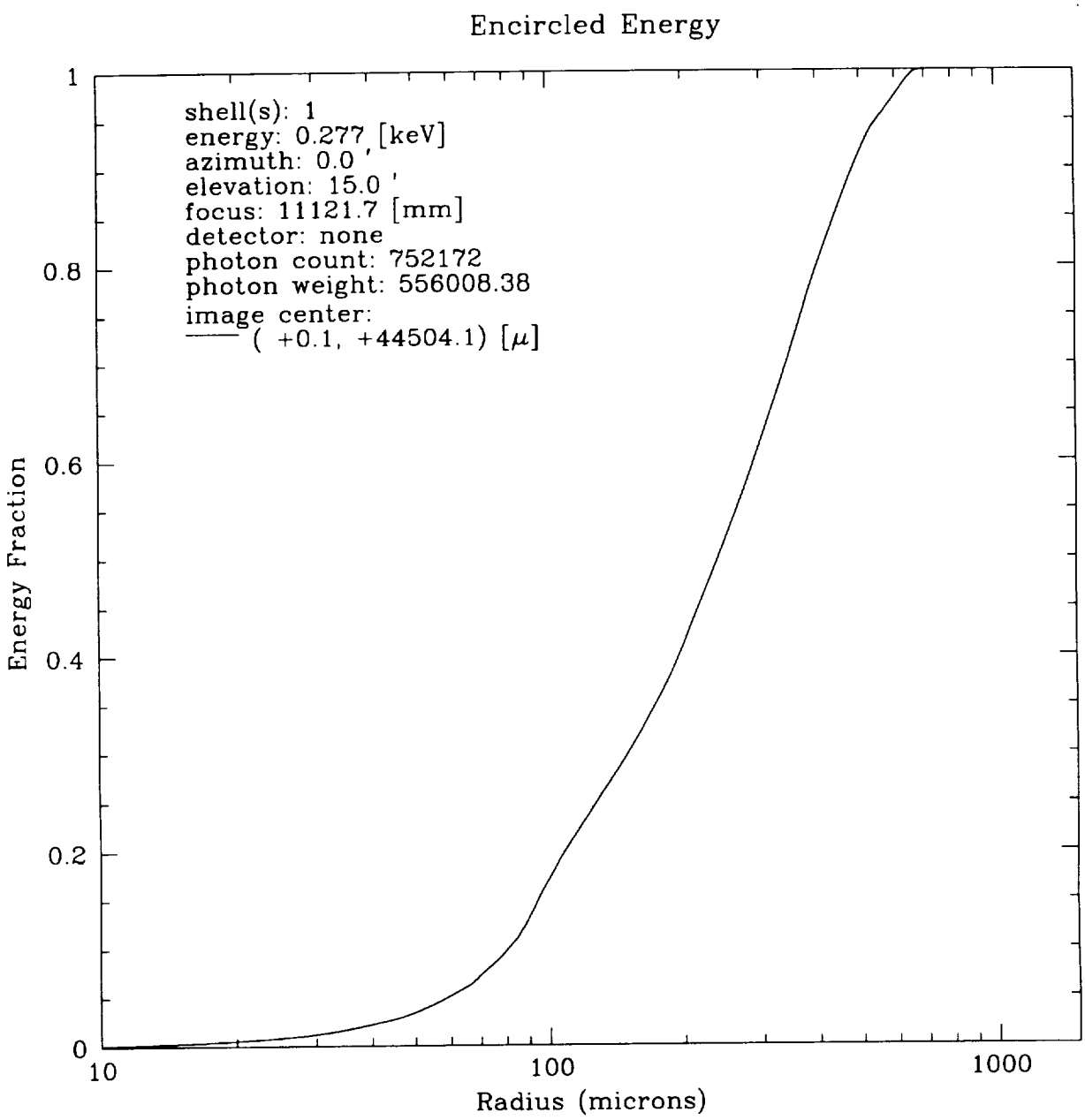
Encircled Energy
shell(s): 1
energy: 0.277 [keV]
azimuth: 0.0 '
elevation: 15.0 '
focus: 11121.7 [mm]
detector: none
photon count: 752172
photon weight: 556008.38
image center:
(+0.1, +44504.1) [μ]
Energy Fraction
0
0.2
0.4
0.6
0.8
1
10
100
1000
Radius (microns)

Figure A.19:

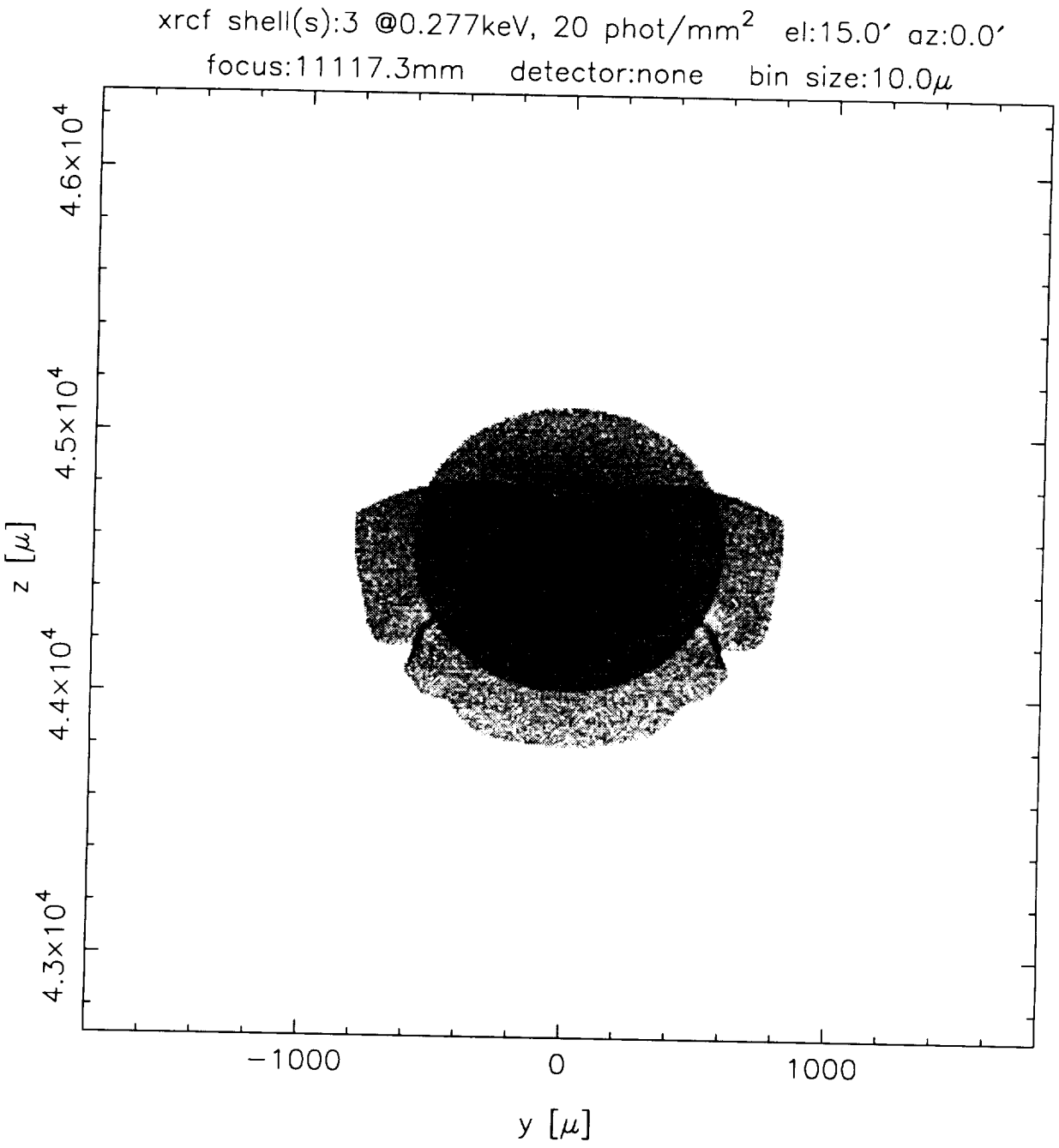
xrcf shell(s):3 @0.277keV, 20 phot/mm^2 el:15.0′ az:0.0′
focus:11117.3mm detector:none bin size:10.0μ
4.6×10^4
4.5×10^4
4.4×10^4
4.3×10^4
z [μ]
−1000
0
1000
y [μ]

Figure A.20:

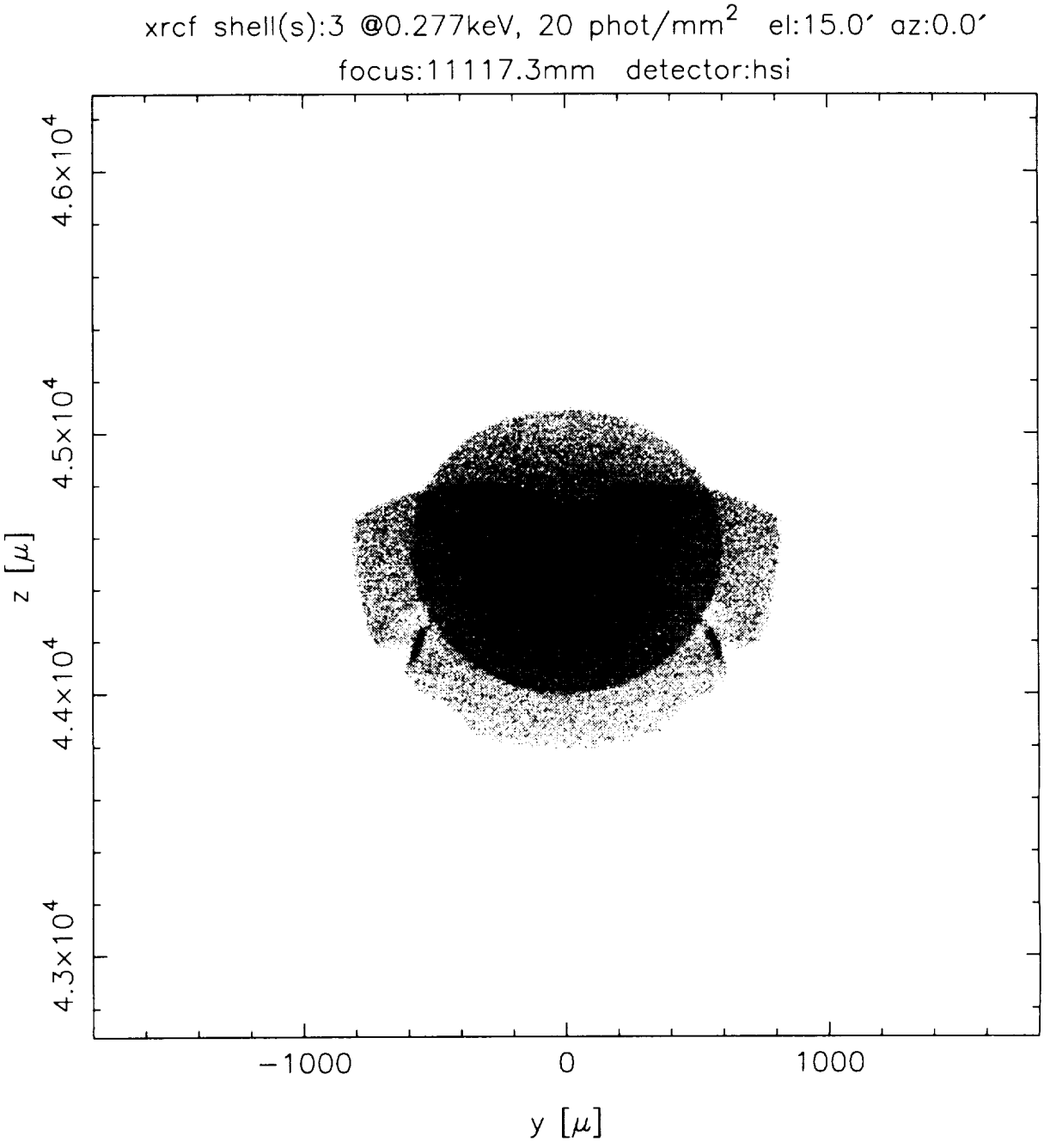
xrcf shell(s):3 @0.277keV, 20 phot/mm^2 el:15.0′ az:0.0′
focus:11117.3mm detector:hsi
4.6×10^4
4.5×10^4
4.4×10^4
4.3×10^4
z [μ]
−1000
0
1000
y [μ]

Figure A.21:

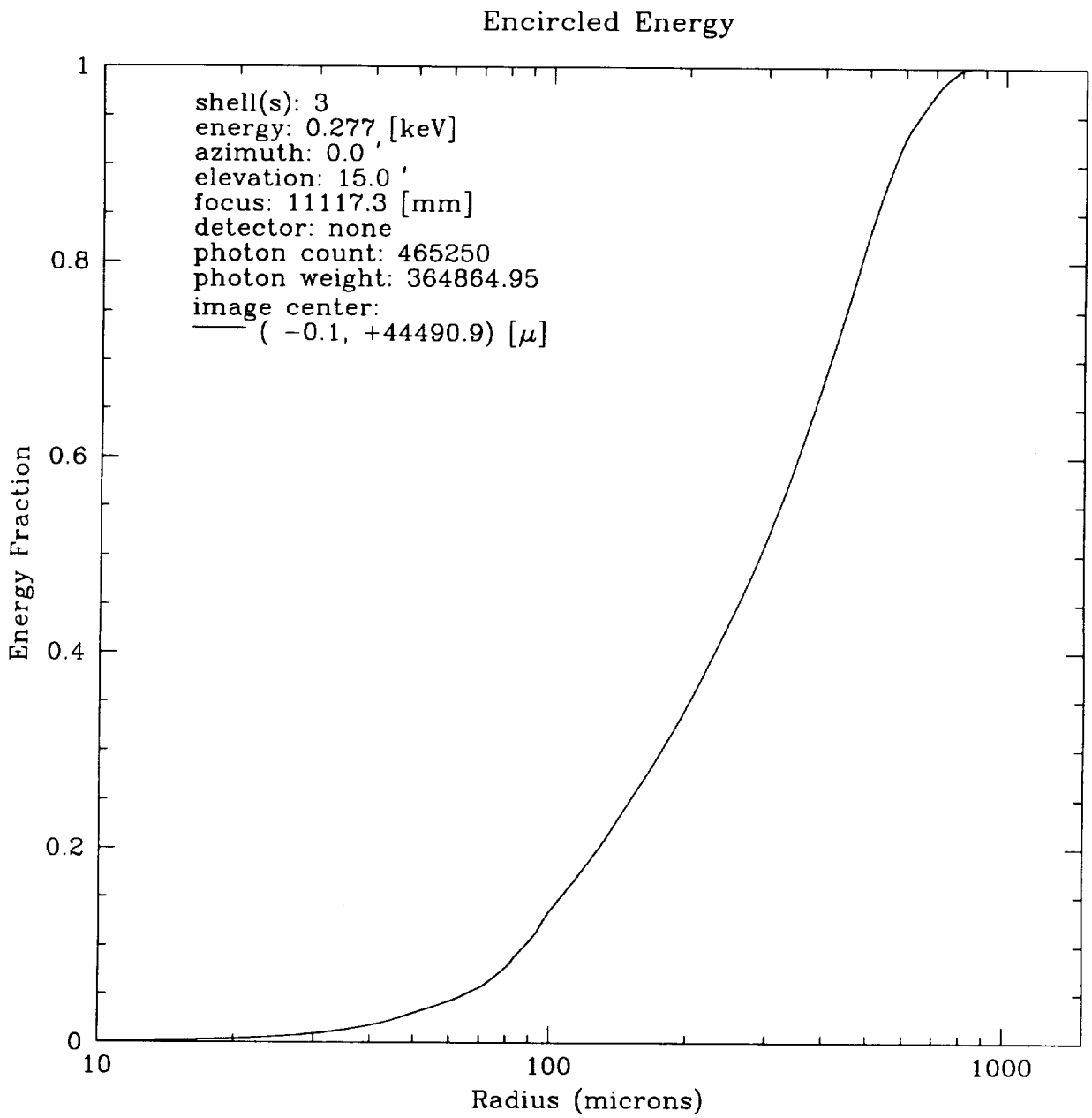
Encircled Energy
shell(s): 3
energy: 0.277 [keV]
azimuth: 0.0 '
elevation: 15.0 '
focus: 11117.3 [mm]
detector: none
photon count: 465250
photon weight: 364864.95
image center:
(−0.1, +44490.9) [μ]
Energy Fraction
0
0.2
0.4
0.6
0.8
1
10
100
1000
Radius (microns)

Figure A.22:

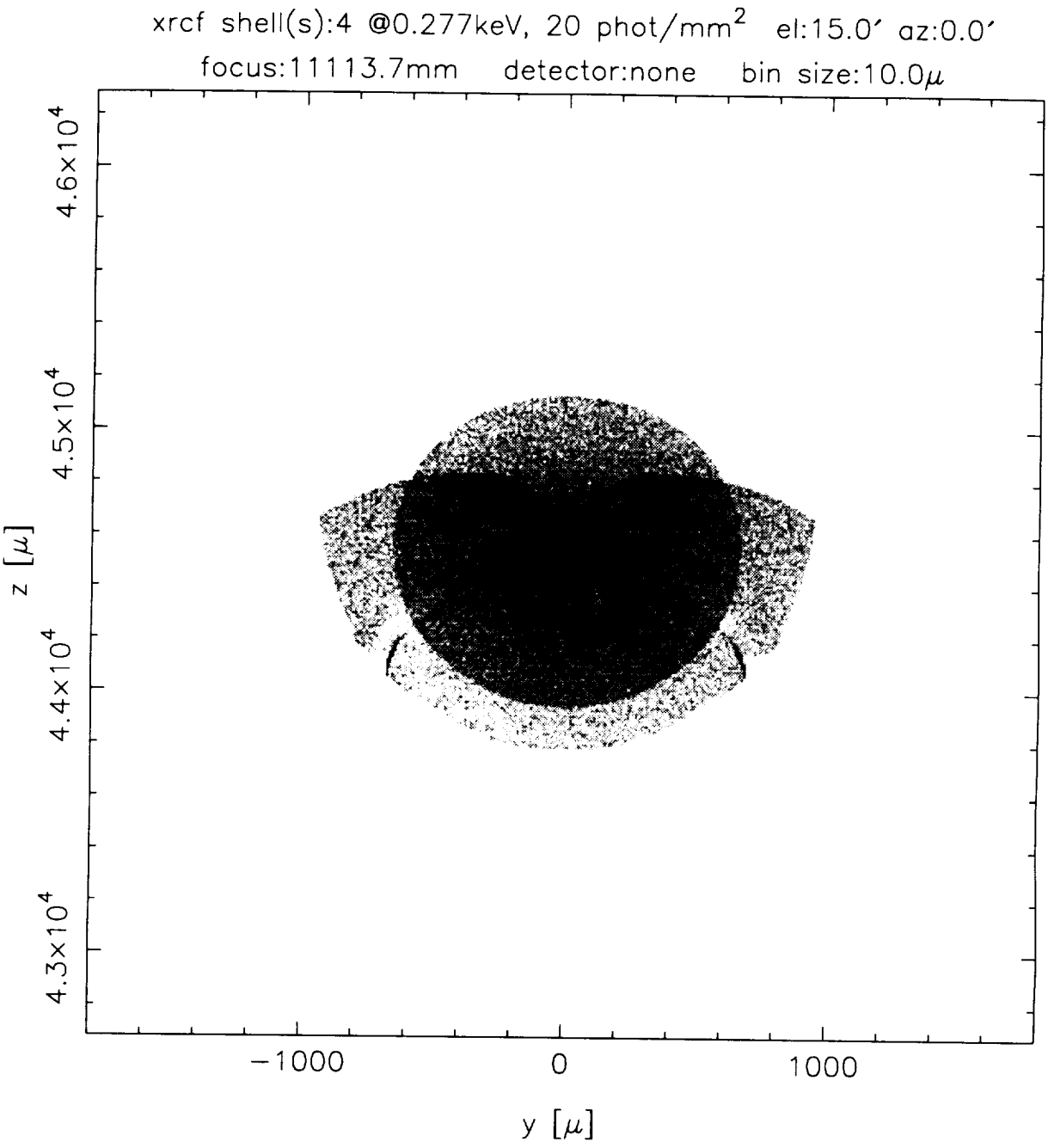
xrcf shell(s):4 @0.277keV, 20 phot/mm^2 el:15.0′ az:0.0′
focus:11113.7mm detector:none bin size:10.0μ
4.6×10^4
4.5×10^4
4.4×10^4
4.3×10^4
z [μ]
−1000
0
1000
y [μ]

Figure A.23:

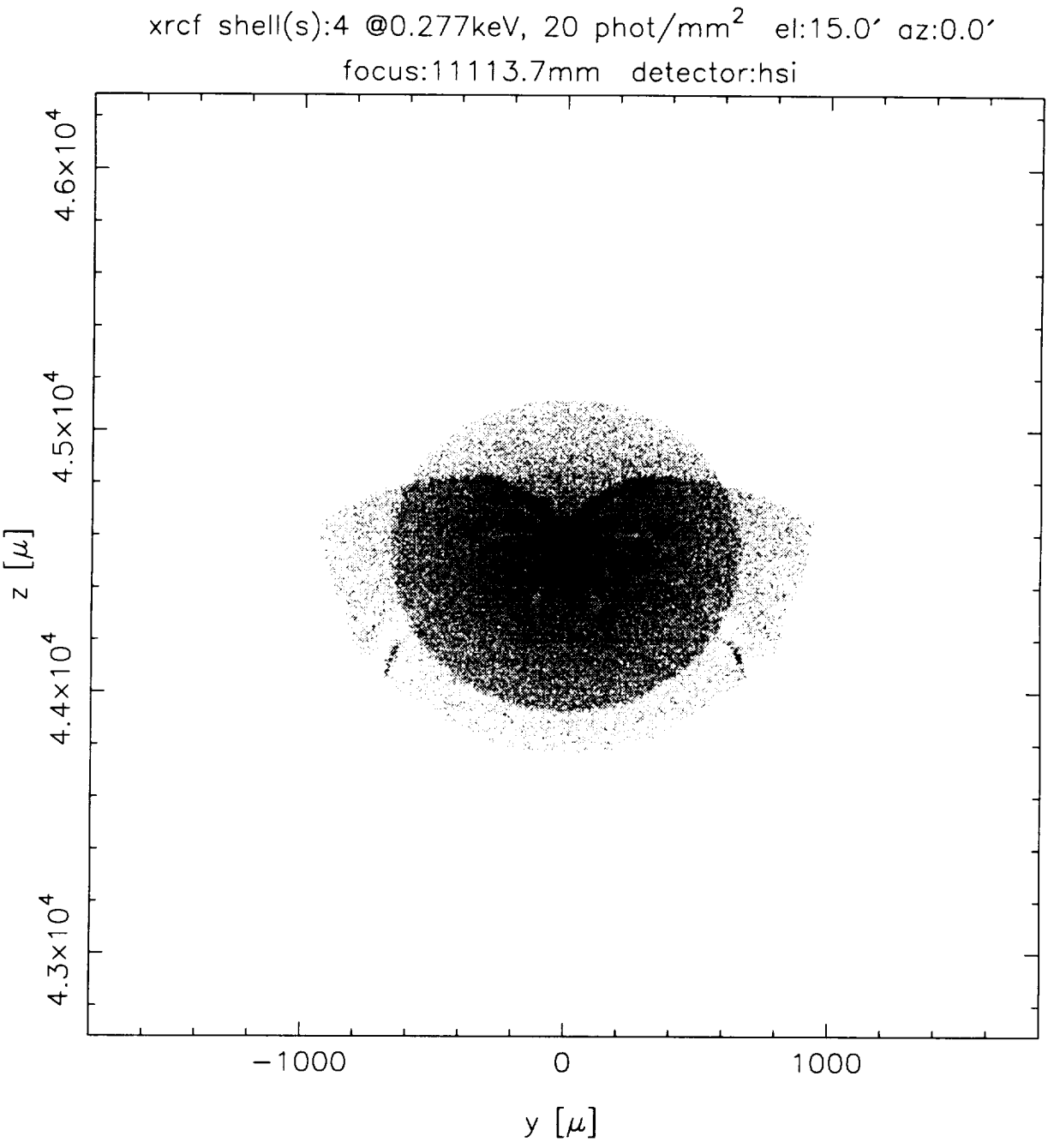
xrcf shell(s):4 @0.277keV, 20 phot/mm^2 el:15.0′ az:0.0′
focus:11113.7mm detector:hsi
4.6×10^4
4.5×10^4
4.4×10^4
4.3×10^4
z [μ]
−1000
0
1000
y [μ]

Figure A.24:

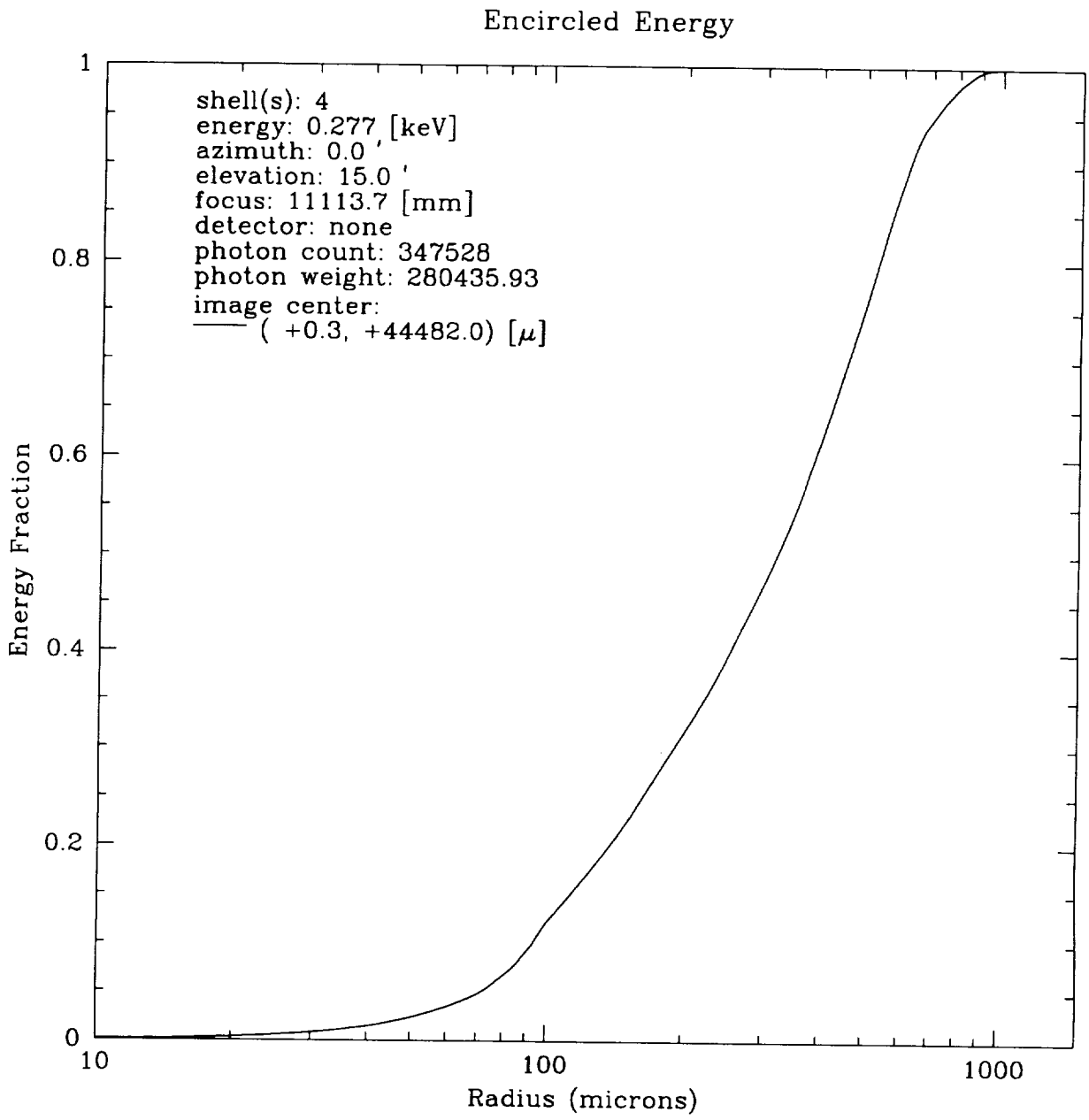
Encircled Energy
shell(s): 4
energy: 0.277 [keV]
azimuth: 0.0 '
elevation: 15.0 '
focus: 11113.7 [mm]
detector: none
photon count: 347528
photon weight: 280435.93
image center:
(+0.3, +44482.0) [μ]
Energy Fraction
0
0.2
0.4
0.6
0.8
1
10
100
1000
Radius (microns)

Figure A.25:

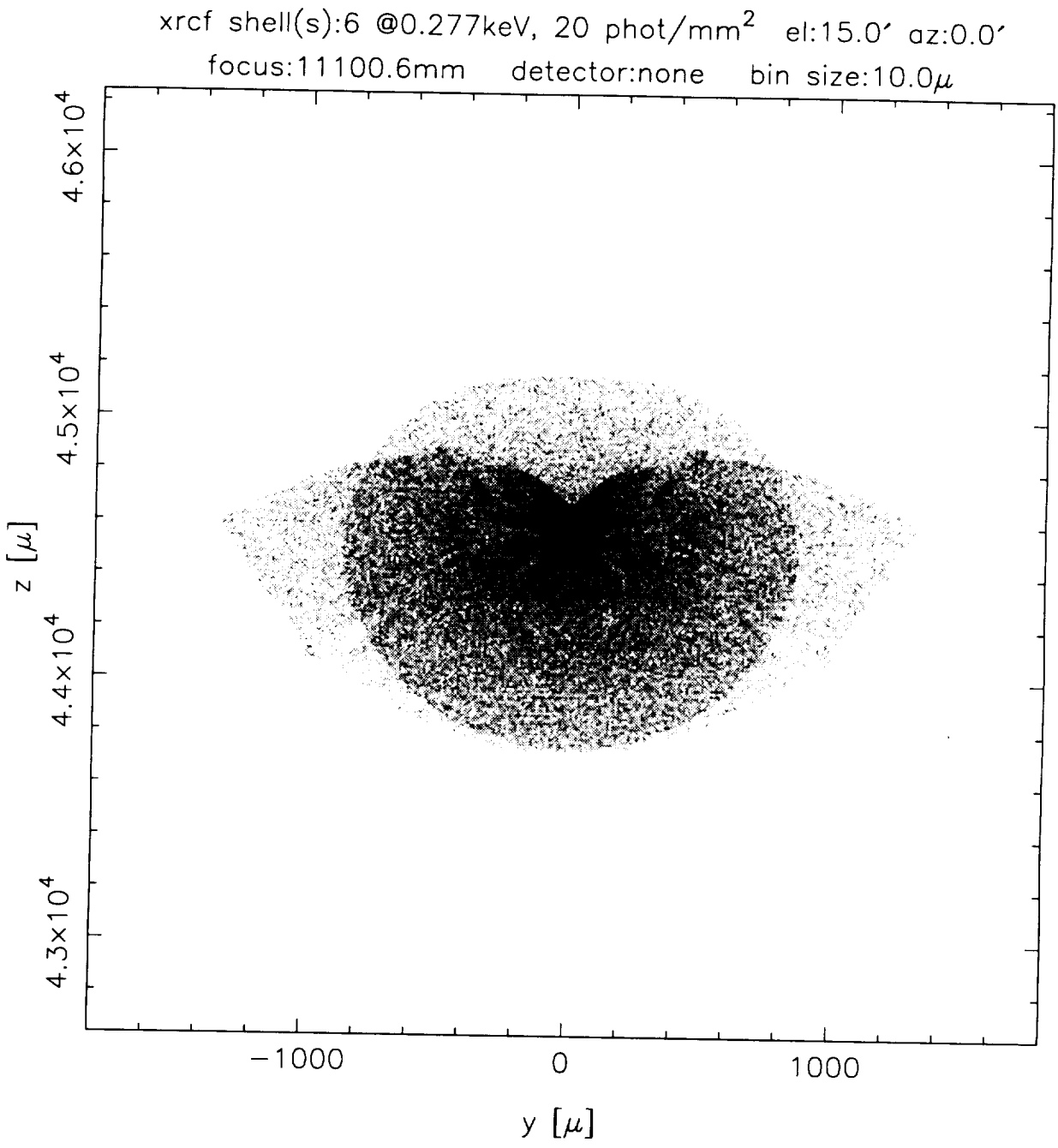
xrcf shell(s):6 @0.277keV, 20 phot/mm^2 el:15.0′ az:0.0′
focus:11100.6mm detector:none bin size:10.0μ
4.6×10^4
4.5×10^4
4.4×10^4
4.3×10^4
z [μ]
−1000
0
1000
y [μ]

Figure A.26:

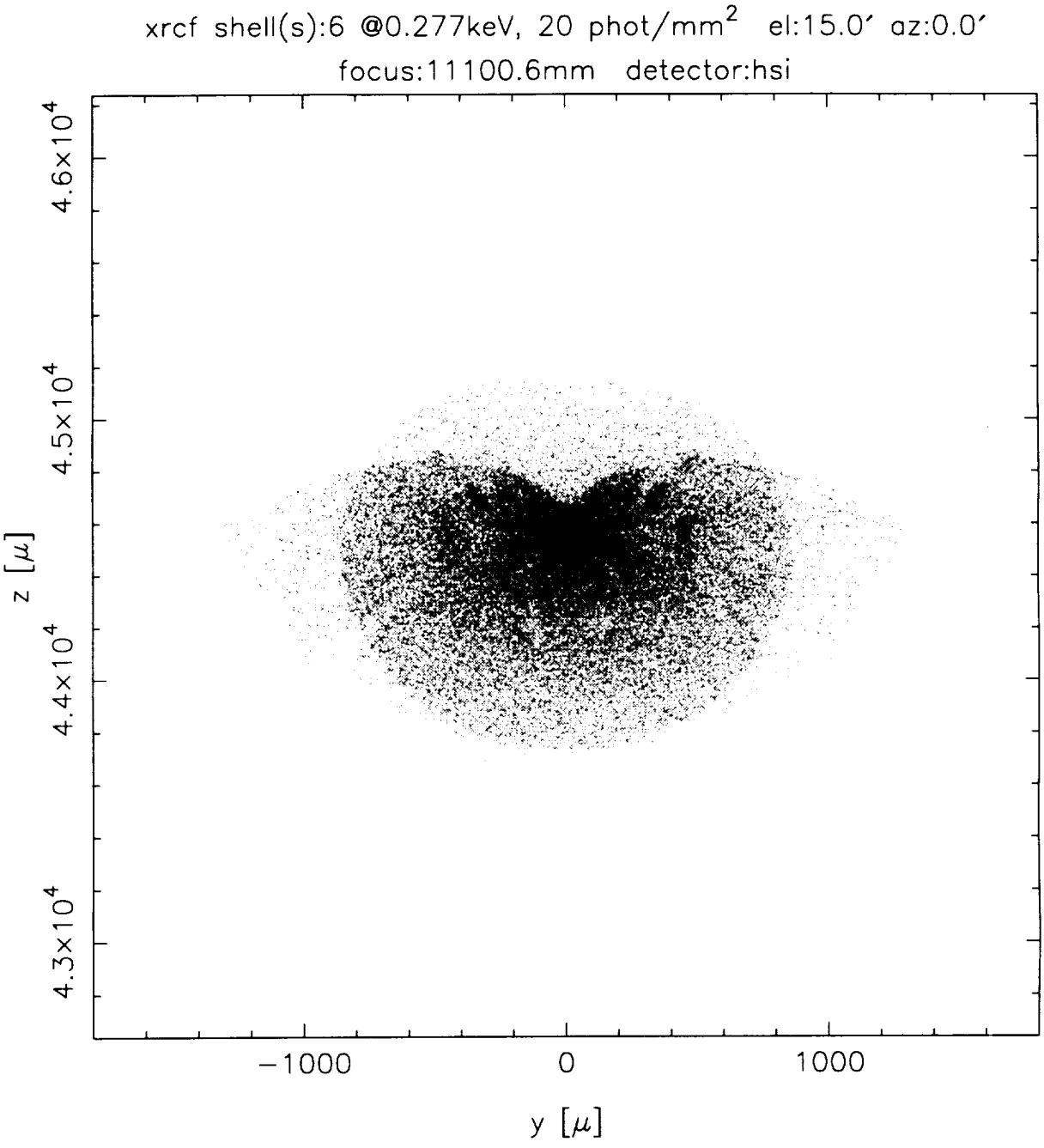
xrcf shell(s):6 @0.277keV, 20 phot/mm^2 el:15.0′ az:0.0′
focus:11100.6mm detector:hsi
4.6×10^4
4.5×10^4
4.4×10^4
4.3×10^4
z [μ]
−1000
0
1000
y [μ]

Figure A.27:

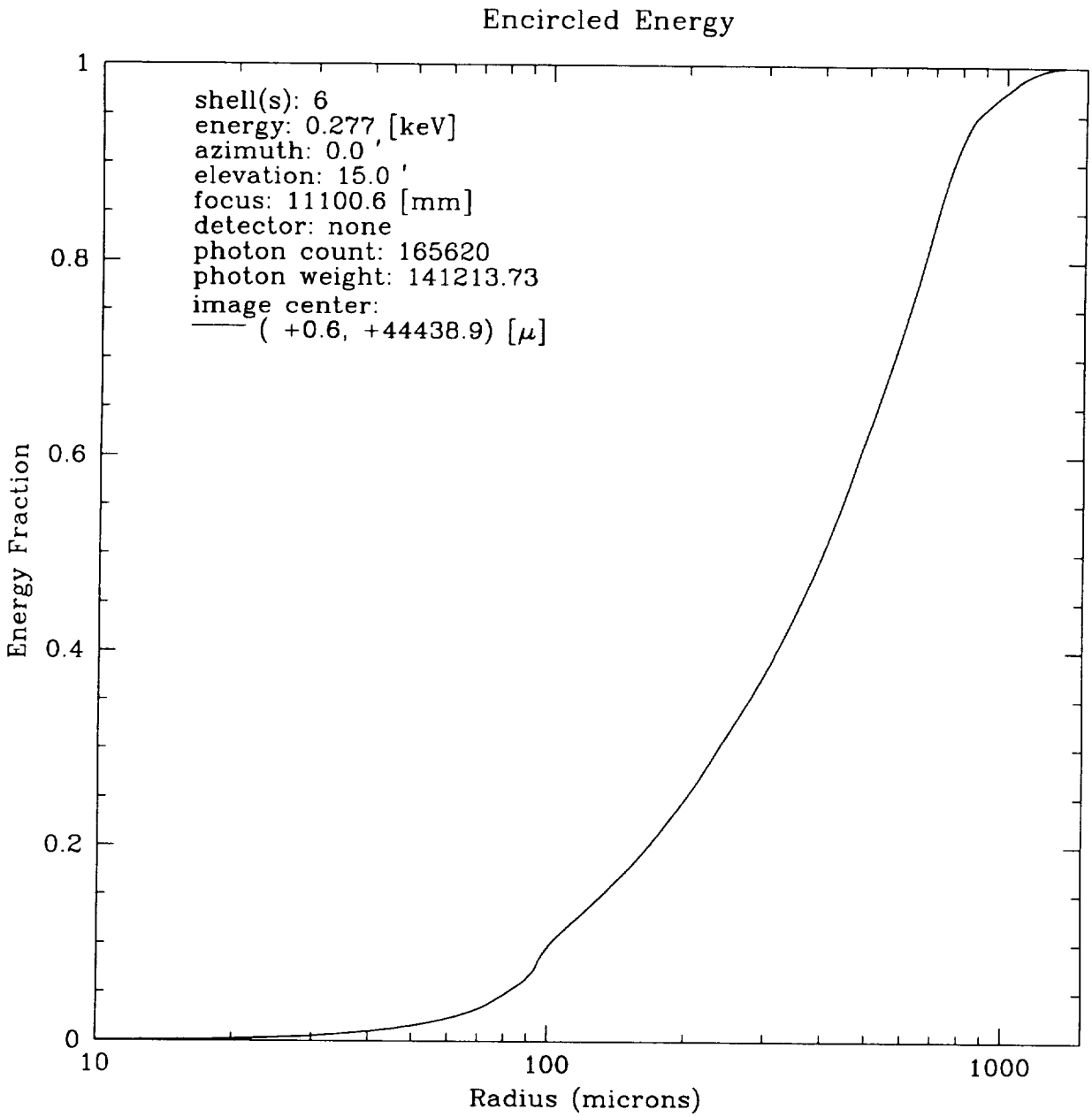
Encircled Energy
shell(s): 6
energy: 0.277 [keV]
azimuth: 0.0 '
elevation: 15.0 '
focus: 11100.6 [mm]
detector: none
photon count: 165620
photon weight: 141213.73
image center:
(+0.6, +44438.9) [μ]
Energy Fraction
0
0.2
0.4
0.6
0.8
1
10
100
1000
Radius (microns)

Figure A.28:

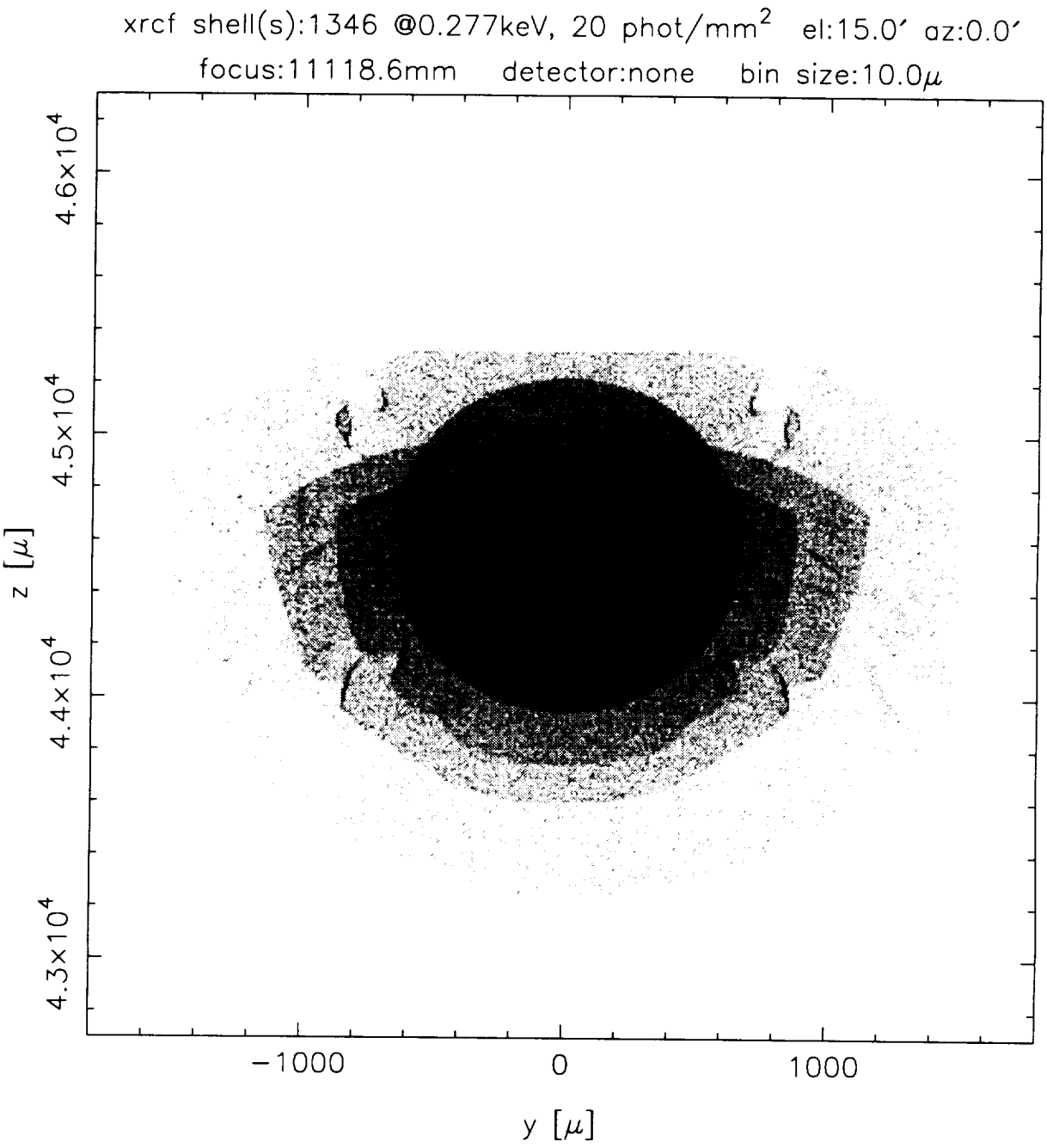
xrcf shell(s):1346 @0.277keV, 20 phot/mm^2 el:15.0′ az:0.0′
focus:11118.6mm detector:none bin size:10.0μ
4.6×10^4
4.5×10^4
4.4×10^4
4.3×10^4
z [μ]
−1000
0
1000
y [μ]

Figure A.29:

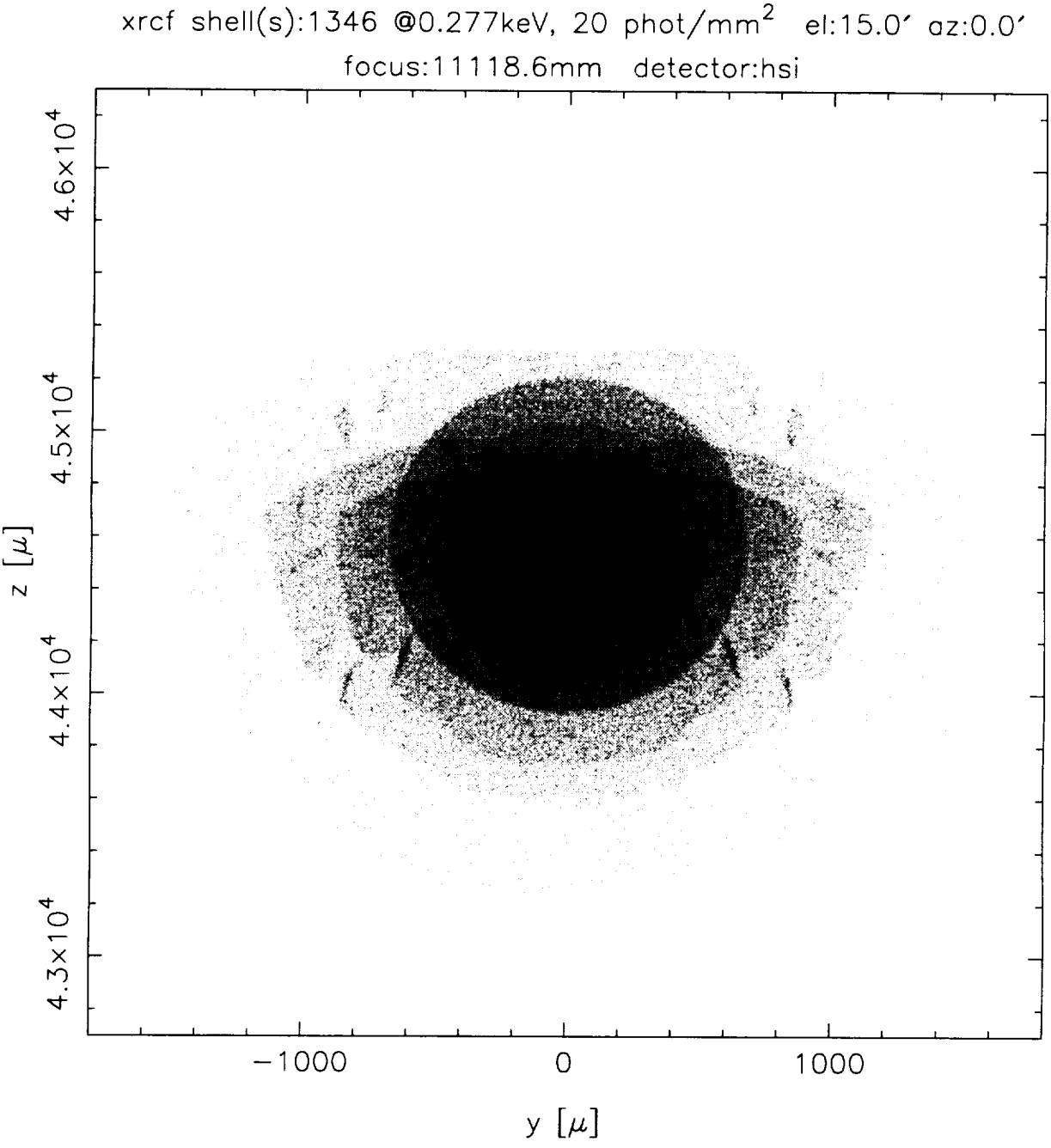
xrcf shell(s):1346 @0.277keV, 20 phot/mm^2 el:15.0′ az:0.0′
focus:11118.6mm detector:hsi
4.6×10^4
4.5×10^4
4.4×10^4
4.3×10^4
z [μ]
−1000
0
1000
y [μ]

Figure A.30:

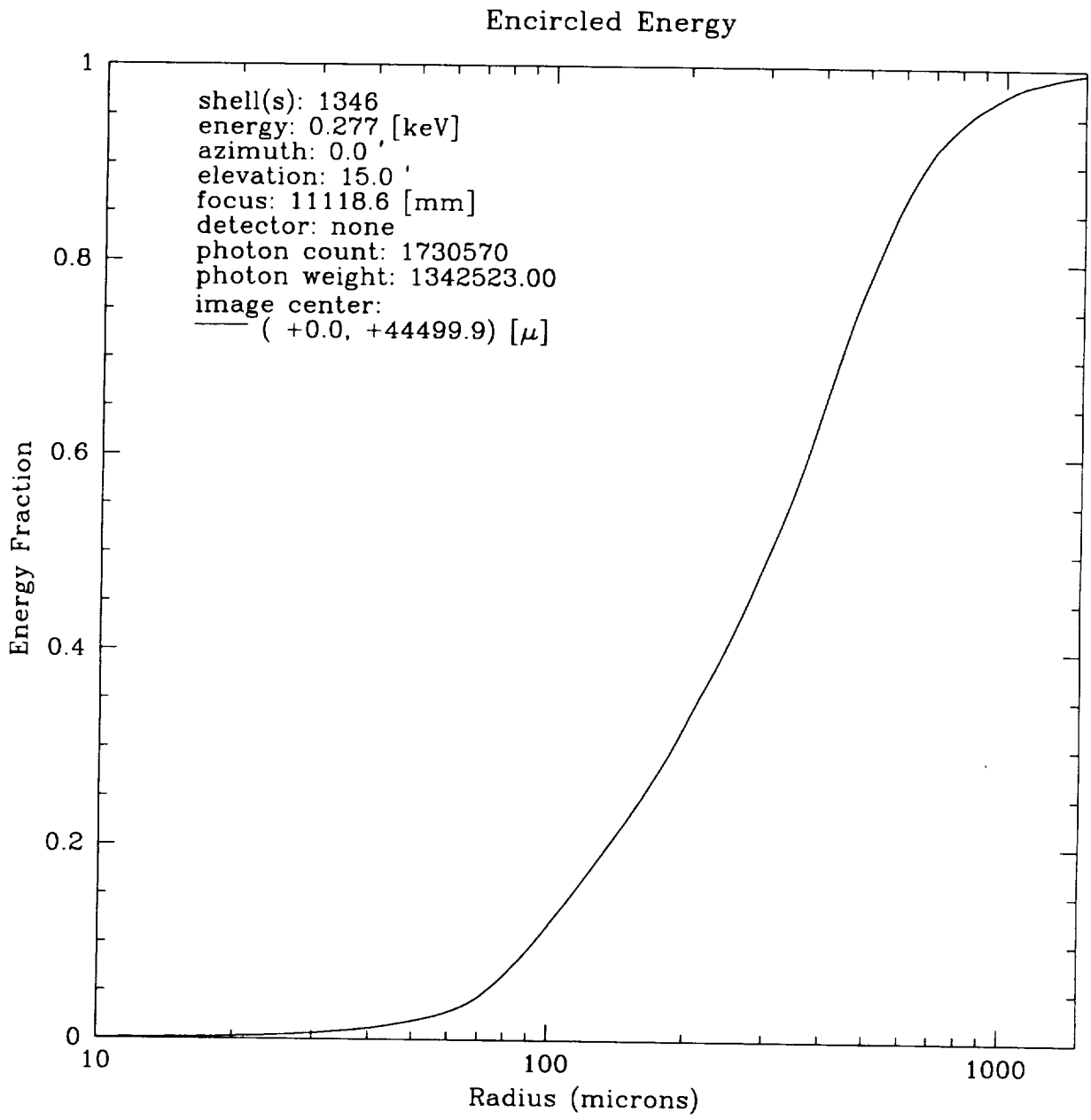
Encircled Energy
shell(s): 1346
energy: 0.277 [keV]
azimuth: 0.0 '
elevation: 15.0 '
focus: 11118.6 [mm]
detector: none
photon count: 1730570
photon weight: 1342523.00
image center:
(+0.0, +44499.9) [μ]
Energy Fraction
0
0.2
0.4
0.6
0.8
1
10
100
1000
Radius (microns)

Figure A.31:

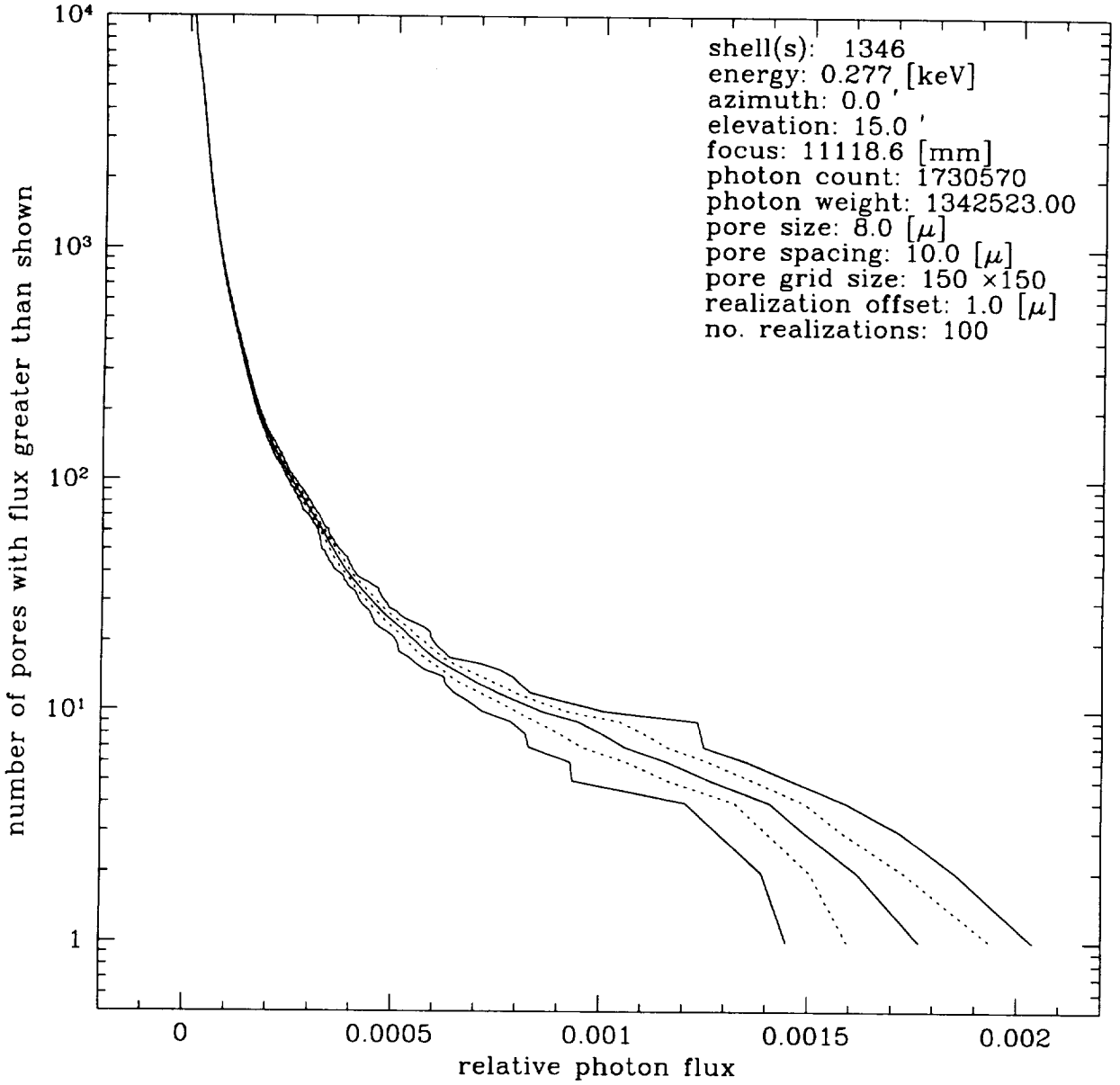
shell(s): 1346
energy: 0.277 [keV]
azimuth: 0.0 '
elevation: 15.0 '
focus: 11118.6 [mm]
photon count: 1730570
photon weight: 1342523.00
pore size: 8.0 [μ]
pore spacing: 10.0 [μ]
pore grid size: 150 ×150
realization offset: 1.0 [μ]
no. realizations: 100
number of pores with flux greater than shown
relative photon flux
10⁴
10³
10²
10¹
1
0
0.0005
0.001
0.0015
0.002

Figure A.32:

Table A.3: Encircled energy fractions for:
xrcf @ 0.277KeV; Azimuth: 0.00′, Elevation: 15.00′

radius (mm) (focus (mm))	shell 1 (11121.7)	shell 3 (11117.3)	shell 4 (11113.7)	shell 6 (11100.6)	HRMA (11118.6)
0.005	0.00032	0.00028	0.00022	0.00008	0.00019
0.010	0.00129	0.00108	0.00087	0.00060	0.00070
0.015	0.00297	0.00231	0.00191	0.00137	0.00153
0.020	0.00530	0.00407	0.00336	0.00228	0.00274
0.025	0.00817	0.00641	0.00548	0.00373	0.00433
0.030	0.01193	0.00948	0.00805	0.00540	0.00635
0.035	0.01668	0.01305	0.01105	0.00757	0.00876
0.040	0.02194	0.01778	0.01442	0.00993	0.01167
0.045	0.02754	0.02370	0.01887	0.01268	0.01522
0.050	0.03439	0.03047	0.02365	0.01578	0.01914
0.060	0.05164	0.04275	0.03442	0.02332	0.02879
0.070	0.07258	0.05681	0.04687	0.03285	0.04384
0.080	0.09807	0.07795	0.06607	0.04770	0.06703
0.090	0.13211	0.10426	0.09034	0.06459	0.09224
0.100	0.17252	0.13535	0.12097	0.09656	0.11880
0.150	0.29947	0.24880	0.22424	0.17642	0.22874
0.200	0.41039	0.34459	0.31592	0.24773	0.32453
0.250	0.52201	0.43368	0.39511	0.31698	0.41084
0.300	0.62177	0.51620	0.47088	0.37780	0.49334
0.350	0.71466	0.59862	0.54236	0.43941	0.56942
0.400	0.79890	0.67861	0.61802	0.49932	0.64956
0.450	0.86323	0.75394	0.68951	0.56049	0.72188
0.500	0.91523	0.82567	0.75741	0.62026	0.77923
0.550	0.95010	0.88265	0.82353	0.67453	0.82460
0.600	0.97360	0.92658	0.88016	0.72789	0.86304
0.650	0.99457	0.95252	0.92481	0.78136	0.89209
0.700	1.00000	0.97418	0.94919	0.83537	0.91527
0.750	1.00000	0.98922	0.96773	0.88362	0.93005
0.800	1.00000	0.99842	0.98136	0.91961	0.94273
0.850	1.00000	1.00000	0.99112	0.94402	0.95292
0.900	1.00000	1.00000	0.99754	0.95616	0.96065
0.950	1.00000	1.00000	0.99990	0.96579	0.96724
1.000	1.00000	1.00000	1.00000	0.97407	0.97306
1.500	1.00000	1.00000	1.00000	1.00000	0.99606
2.000	1.00000	1.00000	1.00000	1.00000	1.00000

This page intentionally left blank

B. An Analysis of Image Structure

While much of the detail in the images presented in Appendix A will not be resolved at the XRCF, it is still important to understand its origin. We present here an analysis of the raytrace through MP6, which shows most clearly the results of what we believe to be an effect common to all of the mirror pairs.

Fig. A.10 shows an image of the rays at best focus for the finite source distance at the XRCF. To remove the effect of the source distance, a raytrace with the source at infinity was run; the image is shown in Fig. B.1. The "wing like" patterns arise from distortions in the glass due to the bonded mirror supports. A more substantial discussion of these involves a thorough review of the detailed mechanical model and is not carried out here. The structure resembling a limaçon is similar to that seen in an out of focus image of a mirror pair with a relative tilt between the hyperboloid and the paraboloid. An illustration of the effects of such a tilt upon images is shown in Fig. B.2. In this instance a set of perfect paraboloidal and hyperboloidal mirrors with a 1 second of arc relative tilt and a source at infinity were raytraced; the images at best focus as well as at various out of focus axial positions are shown in the figure. For comparison, Fig. B.3 shows the raytrace illustrated in Fig. B.1 at a axial position 1mm in front of the best focus. Note that while a "tilt loop" is indeed in evidence, there is a second ring which can be shown to have the same "tilt loop" structure when projected to another axial location.

The presence of *two* "tilt loops" is somewhat surprising, as only one is expected from the geometry. The key to the mystery is that the mirrors are not acting as rigid bodies, but are in fact sagging about the plane containing the bonded mirror support pads. This sagging results in the front and back halves of each mirror acting essentially as independent pieces of glass; there are thus *two* relative tilts – between the front of the paraboloid and the back of the hyperboloid as well as between the back of the paraboloid and the front of the hyperboloid – and thus two resultant tilt limaçons. A clearer illustration of this is shown in Fig. B.4 which shows spot diagrams of the rays which are incident upon the back, middle, and front of the paraboloid.

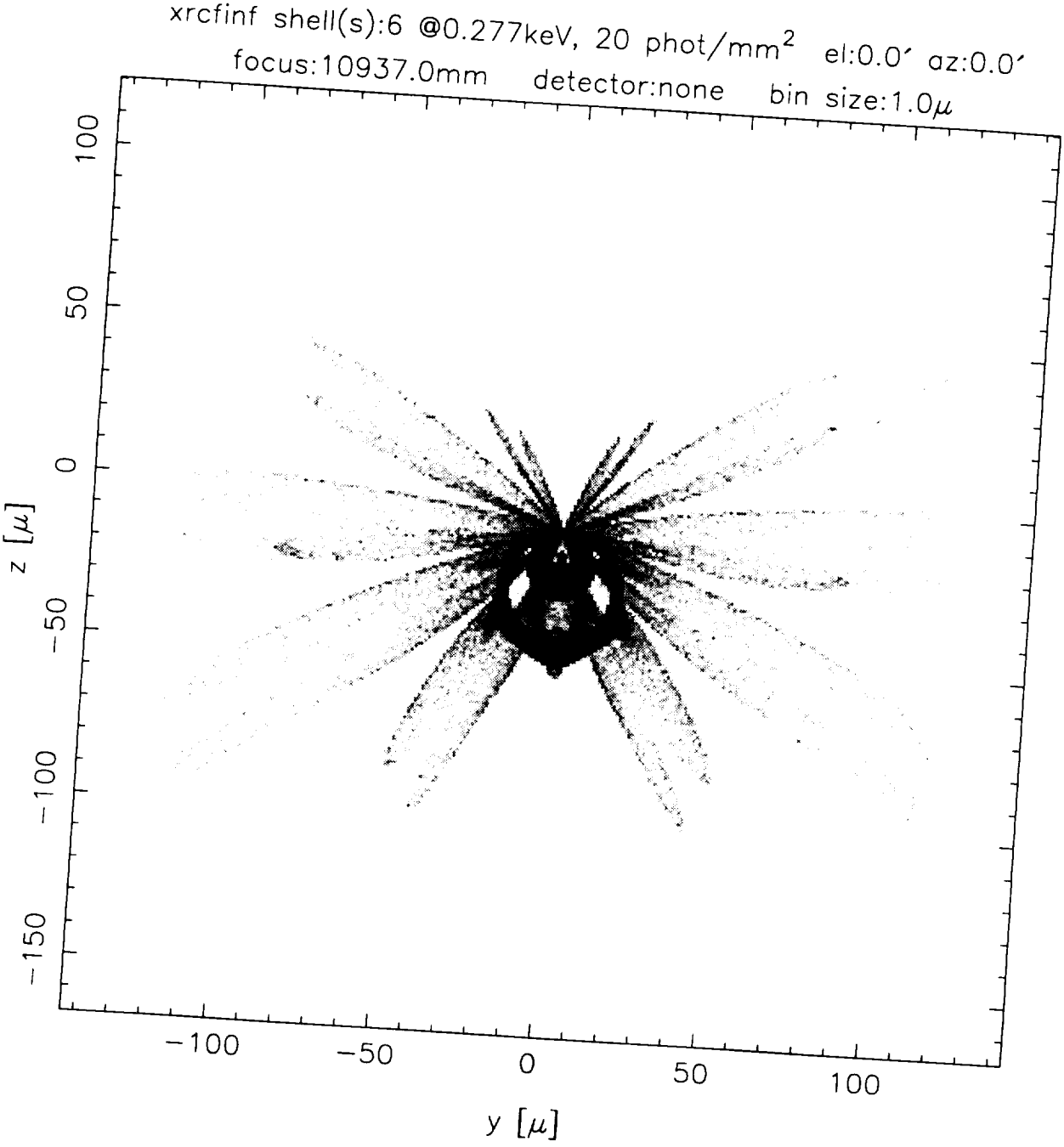

Figure B.1: MP6 with an infinite source distance, at best focus.

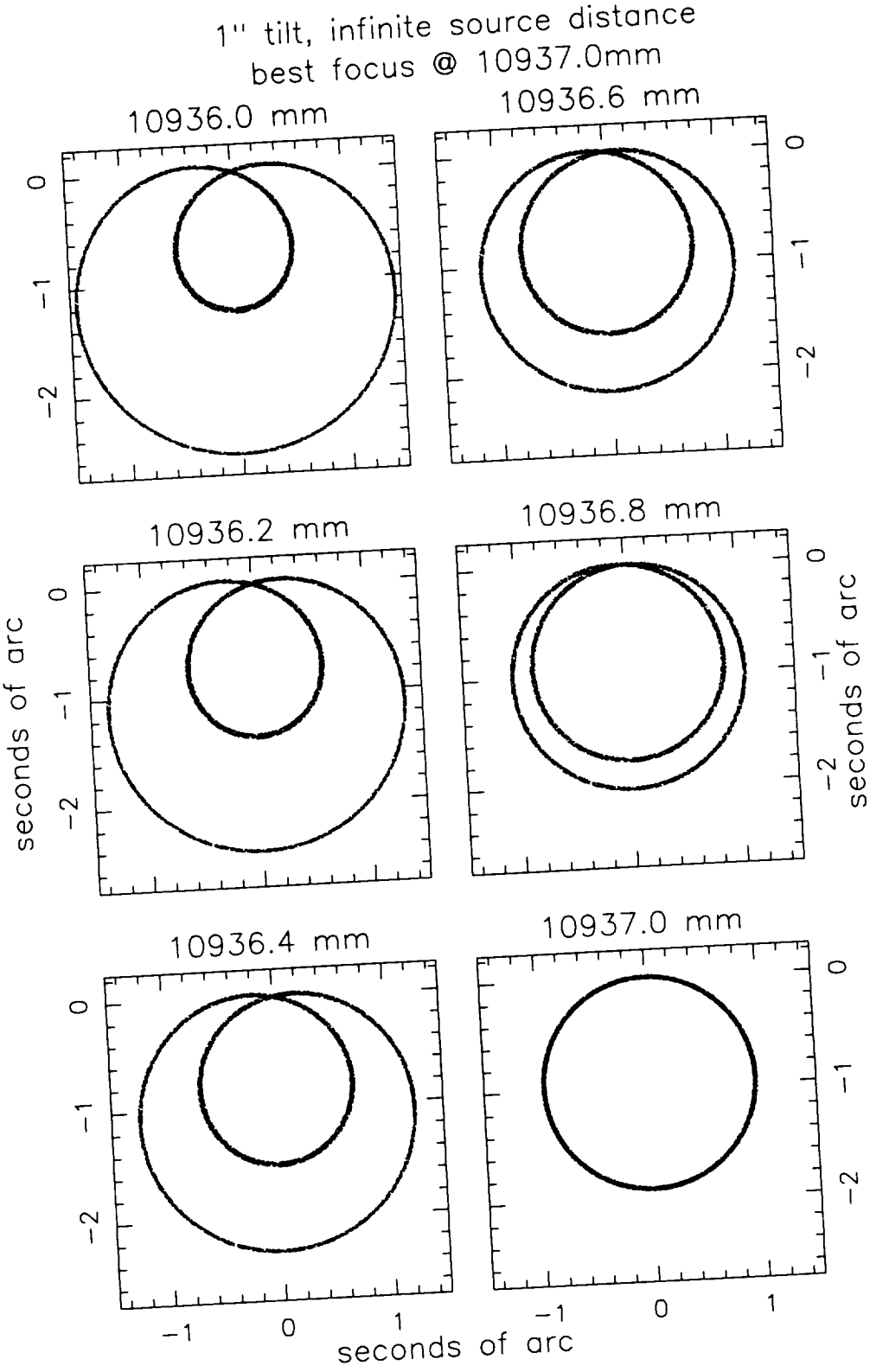

Figure B.2: The effect of a relative tilt upon out of focus images

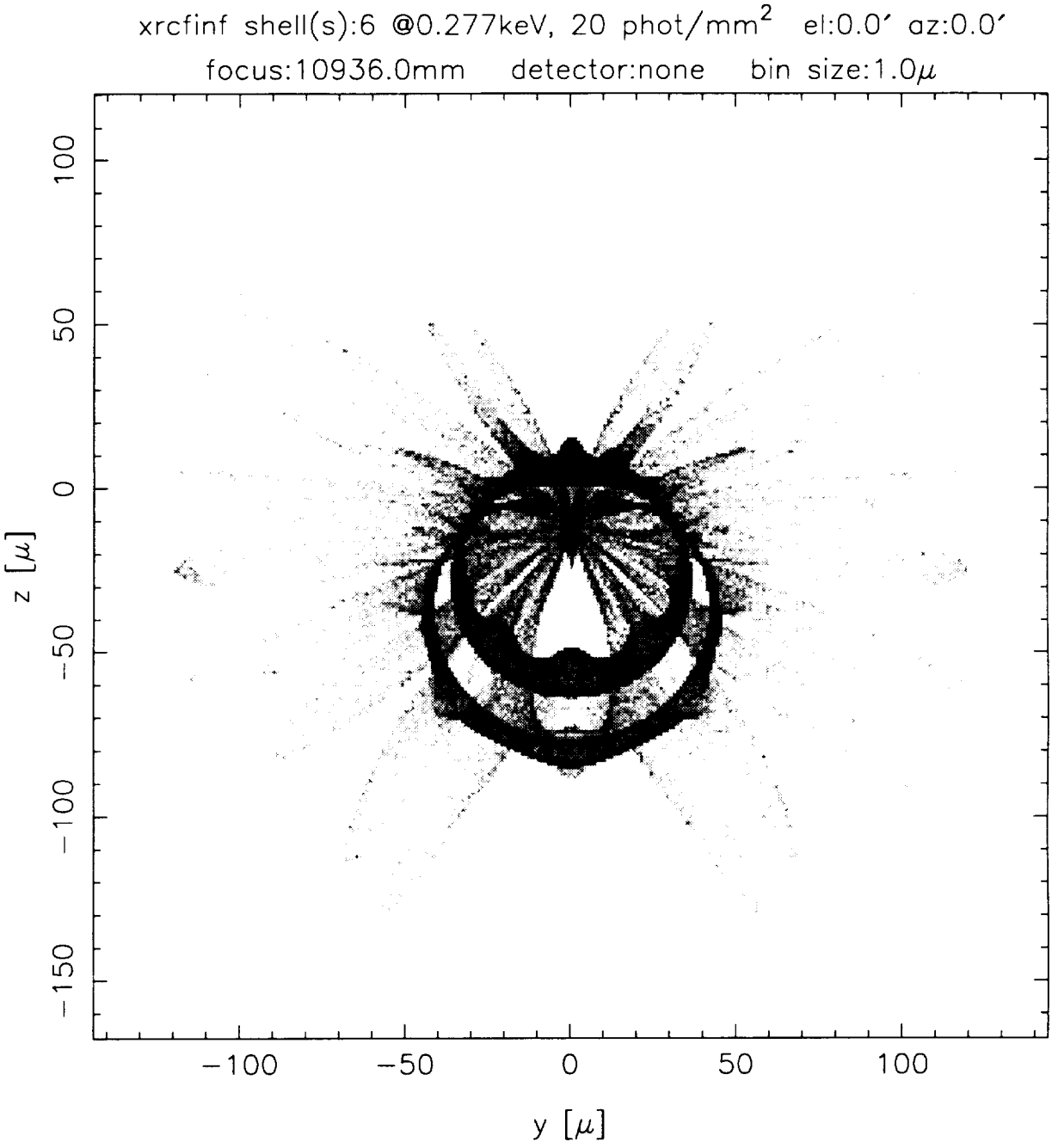

Figure B.3: MP6 with an infinite source distance, 1mm in front of best focus.

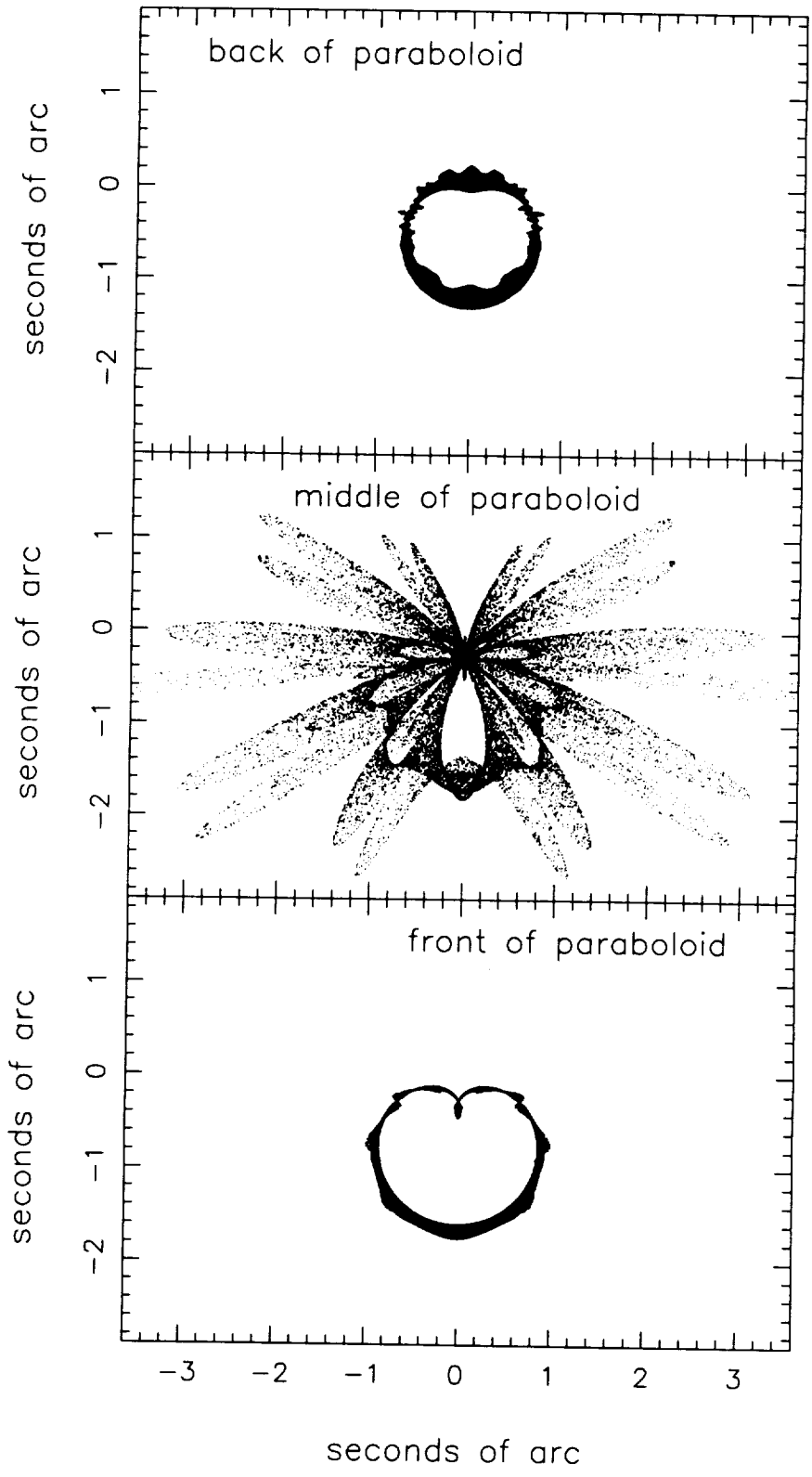

Figure B.4: MP6 source at infinity, 1mm in front of best focus

C. Glossary

AXAF	The Advanced X-ray Astronomical Facility
CAP	Central Aperture Plate – the plate to which the mirror support sleeves are attached
EKC	Eastman Kodak Company
FEM	Finite element model
FEA	Finite element analysis
FWHM	Full-Width at Half Maximum
GSE	Ground Support Equipment
HRMA	High Resolution Mirror Assembly – the combination of the mirrors, their support structures, and the fore- and aft- structures.
HSI	High Speed Imager – a micro-channel plate based detector to be used at the XRCF to test the HRMA.
HXDS	HRMA X-ray Detector System
MP	Mirror Pair – a pair of paraboloidal and hyperboloidal mirrors which make up one of the four nested shells of AXAF.
MSFC	Marshall Space Flight Center
MST	Mission Support Team
NASTRAN	Commercial FEA code
SAOsac	SAO's updated version of OSAC's `drat` routine, which includes B-spline optic deformations as well as improved i/o performance via UNIX pipes.
OSAC	Optical Surface Analysis Code – a ray tracing code capable of dealing with grazing incidence optics and deformed optics, developed at Perkin-Elmer for NASA.
`perl`	Practical Extraction and Report Language – a language designed to easily manipulate text and databases. It provides a superset of the functionality of the UNIX tools `awk`, `sed`, and `grep`, as well as

	providing easy access to UNIX kernel functions and inter-process-communications.
PSF	Point Spread Function
SAO	Smithsonian Astrophysical Observatory
TBD	To Be Determined
TRANSFIT	GUI-driven software for fitting continuous surface functions to FEA data of cylindrical optics.
UNIX	A multi-user, multi-tasking (and possibly multi-processing) operating system.
VETA-I	Verification Engineering Test Article I – the pre- end cut paraboloidal and hyperboloidal mirrors which make up AXAF's outer mirror shell.
XRCF	X-Ray Calibration Facility – the facility at MSFC where the HRMA will be calibrated.

D. FEM files

The mechanical model used by these simulations is parameterized as a set of B-splines. The coefficients can be found in the directory

`/proj/axaf/Syseng/models/hrma-xrcf/1G/offloaded/EKC` as

- `hrma-xrcf_p1.SPL`
- `hrma-xrcf_h1.SPL`
- `hrma-xrcf_p3.SPL`
- `hrma-xrcf_h3.SPL`
- `hrma-xrcf_p4.SPL`
- `hrma-xrcf_h4.SPL`
- `hrma-xrcf_p6.SPL`
- `hrma-xrcf_h6.SPL`

These files were derived from the Kodak FEA model output `hrma-xrcf.pch`, transferred to SAO on 23 September, 1993.